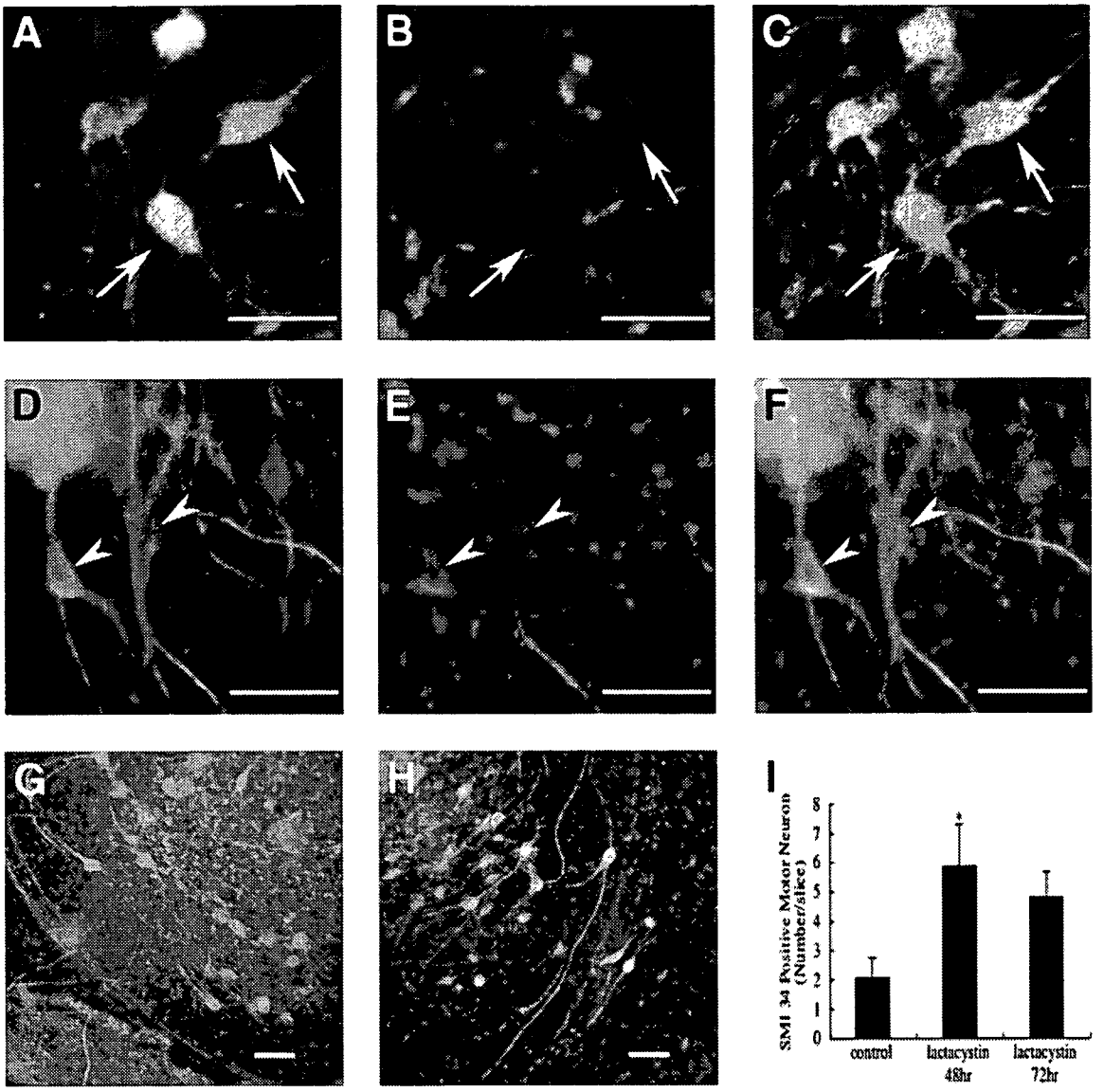

Fig. 4. Phosphorylated neurofilaments increased after lactacystin exposure. **A–F:** In double immunofluorescence of SMI-31 and SMI-34, motor neurons (arrows) were not phosphorylated without lactacystin (A–C). SMI-31-positive motor neurons (arrowheads) increased after 5 μM lactacystin exposure for 36 hr (d-f). A, D: SMI-32. B, E: SMI-34. C, F: Merge. G, H: In double immunofluorescence of SMI-32 (green) and -34 (red), there were few SMI-34-positive cells in control cultures (G). After a 48-hr exposure, the number of double-positive motor neurons (merge, yellow) increased (H). I: A significant difference was seen in the number of SMI-34-positive neuron after a 48-hr exposure compared to control $*P < 0.05$.

ing motor neurons as SMI-32-positive cells located in the anterior horns, having large somas (>30 μm) and long processes. To clarify a differential effect of the proteasome inhibitor we exposed organotypic slice cultures of the spinal cords to the irreversible proteasome inhibitor lactacystin (0.5–5 μM). Decreased proteasome activity was confirmed by measurements after a 3-hr exposure to lactacystin in a dose-dependent manner (Fig. 2). They remained suppressed at the same level of activity for 24 hr.

Thirty-six hours after exposure to 5 μM lactacystin, some of the motor neurons showed morphological changes. The neurites of untreated motor neurons were thick, especially in their origins (Fig. 3A). Lactacystin-exposed neurons were exhibited as thin neurites from their origins and some neurites were fragmented (Fig. 3B). Because it is known that phosphorylated neurofilaments appear in motor neurons in ALS, we examined the double immunohistochemistry with SMI-32 and SMI-31. SMI-32 recognizes a nonphosphorylated neurofilament heavy chain and SMI-31 recognizes a phosphorylated one. In the control slices, SMI-31-positive motor neurons were seldom observed (Fig. 4A–C). In contrast, the lactacystin-treated slices contained some motor neurons, which were double positive for SMI-32 and -31 (Fig. 4D–F). Another

antiphosphorylated neurofilament antibody, SMI-34, was also positive in lactacystin- treated cultures (Fig. 4G,H). Phosphorylation was seen in cell bodies and neurites that occurred in both normal-shaped neurons and degenerated ones. Slice cultures are considered to have dispersion in the number of neurons initially contained in each slice, and mechanical damage by axotomy during preparation induces cell loss even without toxic insults. We concluded that these changes resulted from proteasome impairment, however, because severe neurite fragmentation and phosphorylation of neurofilaments were seldom observed in control cultures. In regard to statistical analysis, SMI-34-positive neurons increased significantly in 48-hr lactacystin-exposed slices (Fig. 4I). We did not find a significant difference between the 72-hr exposed group and control, which we think was due to severe motor neuron loss after a long-term exposure.

Proteasome Dysfunction Induced Specific Death of Motor Neurons

Seventy-two hours after exposure to lactacystin, the number of motor neurons significantly decreased in a 5 μM lactacystin treatment group compared to the control one (Fig. 5A). The remaining cells exhibited atrophic, condensed somas and fragmented meandering neurites (Fig. 5B,C). Some motor neurons had lost their neurites entirely. In contrast, the SMI-32-positive neurons in the dorsal horns showed little change (Fig. 5D,E). The general structure of the dorsal horns was conserved and the thick neurites of large neurons stretched smoothly. To examine the dorsal horn more clearly, we stained it with the anti-calretinin antibody, which is considered to be a marker for dorsal horn neuron. After treatment with 5 μM lactacystin for 72 hr, calretinin-positive neurons showed little morphological change (Fig. 6A,B). The number of surviving motor neurons significantly decreased in a dose-dependent manner (1 μM, $*P < 0.05$; 5 μM, $**P < 0.01$), but the number of calretinin-positive neurons in the dorsal horns did not change ($P > 0.05$; Fig. 7A).

Another specific proteasome inhibitor, epoxomicin, also induced the same degeneration as lactacystin did. Motor neurons were damaged in a dose-dependent manner and showed a significant difference at 50 nM, whereas the dorsal horn neurons did not show any differences (Fig. 7B). We prepared 100 nM epoxomicin-treated slices but could not evaluate them because they were too fragile to be fixed by the free-floating method (only 25% of them could be fixed). Excessive proteasome inhibition might affect not only neurons but also glial cells, which are indispensable for a slice to attach to a membrane.

Motor Neurons Did Not Express Major Calcium-Binding Proteins, Calretinin and Calbindin D-28K

In ALS, the nucleus of extraocular muscles and Onuf's nucleus are spared. One of the major hypotheses

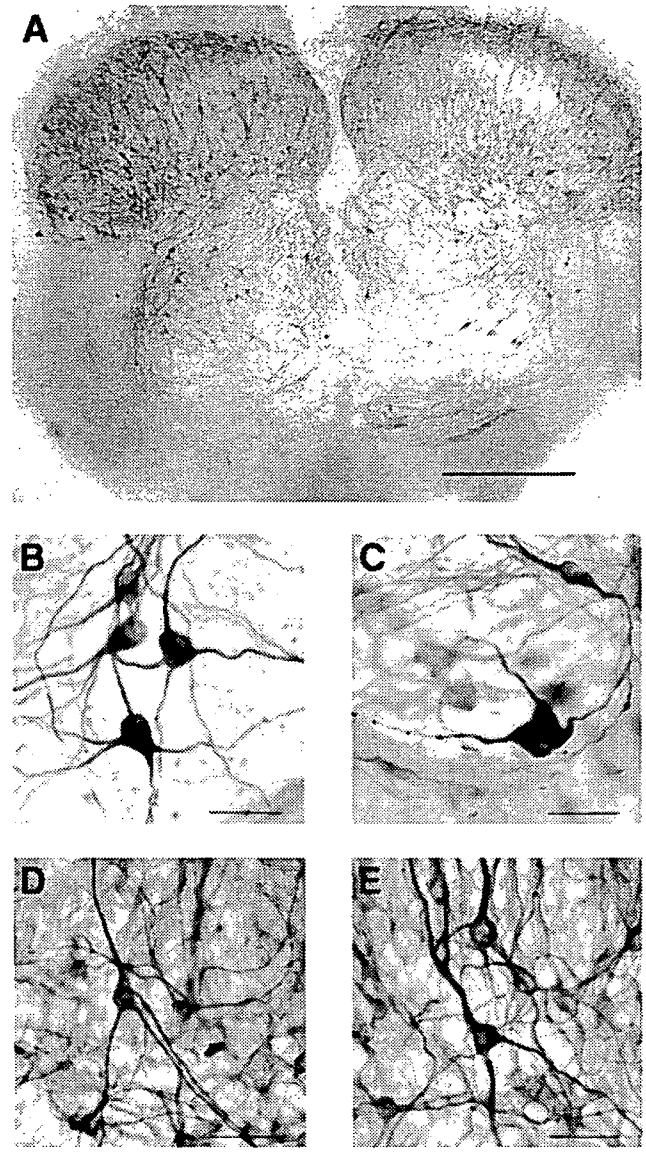

Fig. 5. **A:** SMI-32-immunostaining of whole slice culture treated with 5 μM lactacystin for 72 hr. Severe motor neuronal loss was observed in anterior horns, whereas the construction of dorsal horns was preserved. Scale bar = 400 μm. **B–E:** In a higher-power field, compared to nontreated motor neurons (B), lactacystin-exposed motor neuron looked profoundly degenerative (C). Its neurites were fragmented and winding, the margin of the cell body became irregular. D, E: Large neurons in dorsal horns showed no change. Note neurites, which smoothly stretched in a nontreated slice (D) and a lactacystin-exposed slice (E). B–E: All were the same magnification. Scale bar = 40 μm.

of a differential factor between an easily damaged group of motor neurons and a relatively resistant one is the capacity of Ca^{2+} buffering. Easily damaged groups of motor neurons were reported to lack major calcium-binding proteins (Alexianu et al., 1994), and in a comparative study of the oculomotor nerve, they had a lower capacity of Ca^{2+} buffering (Vanselow and Keller, 2000).

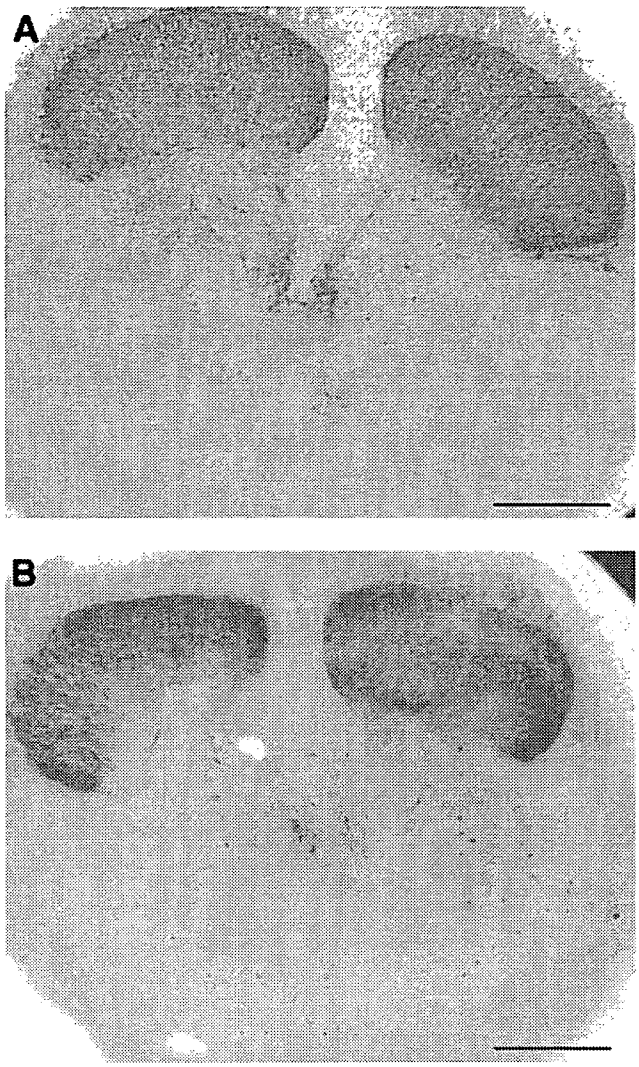

Fig. 6. In calretinin immunohistochemistry, many dorsal horn neurons could be observed. There was little difference between non-treated slices (**A**) and 5 μM lactacystin-exposed slices (**B**).

We examined two Ca^{2+}-binding proteins, calretinin and calbindin D-28K, which have a high capacity for buffering. Motor neurons showed a lack of staining with both calretinin and calbindin D-28K, whereas many posterior horn neurons strongly expressed these proteins (Fig. 8A–E).

Intracellular Ca^{2+} Chelation Ameliorated Lactacystin-Induced Neurotoxicity

To confirm whether the involvement of Ca^{2+} homeostasis could be the key to the specific vulnerability of motor neurons induced by proteasome inhibition, we cotreated slice cultures with lactacystin and an intracellular Ca^{2+} chelator, BAPTA-AM. In addition, other agents affecting intracellular Ca^{2+} concentration were also examined. Cotreatment of BAPTA-AM (10 μM) with lactacystin reduced the degenerated motor neurons significantly ($P < 0.01$; Fig. 9A). Many motor neurons preserved smooth and thick neurites in cotreated cultures (Fig. 9B). The simultaneous treatment with BAPTA-AM did not affect the proteasome inhibition by lactacystin (data not shown).

The NMDA receptor blocker MK-801 (10 μM) and AMPA/kainate receptor blocker CNQX (50 μM) were investigated because excessive synaptic glutamate and defective RNA Q/R-editing of GluR2 might be involved in causing ALS to occur (Rothstein et al., 1993; Kawahara et al., 2004). They had a tendency to ameliorate the lactacystin-induced toxicity but without significance. Ifenprodil (10 μM), a specific blocker of NMDA receptors containing an NR2B subunit, and the L-type Ca^{2+} (20 μM) channel blocker failed to show any protective effects.

DISCUSSION

We showed that proteasome inhibition induced severe degeneration in motor neurons compared to that in posterior neurons. We considered the major reason for this specific vulnerability to be the low ability of calcium buffering. We reported previously that motor neu-

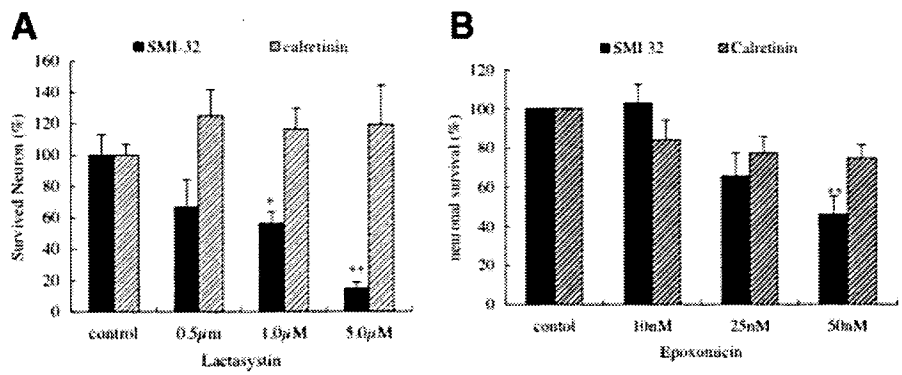

Fig. 7. **A:** After a 72-hr exposure to lactacystin, the number of surviving motor neurons decreased in a dose-dependent manner and had a statistical difference at more than 1 μM (filled bar, $*P < 0.05$, $**P < 0.01$). Calretinin-positive dorsal horn neurons were not damaged significantly at 5 μM (shaded bar, $P < 0.05$). **B:** Epoxomicin-exposed slices showed the same results as lactacystin. Motor neurons decreased in a dose-dependent manner, significantly at 50 nM (filled bar, $**P < 0.01$). On the other hand, calretinin-positive dorsal neurons didn't show any remarkable change (shaded bar, $P > 0.05$).

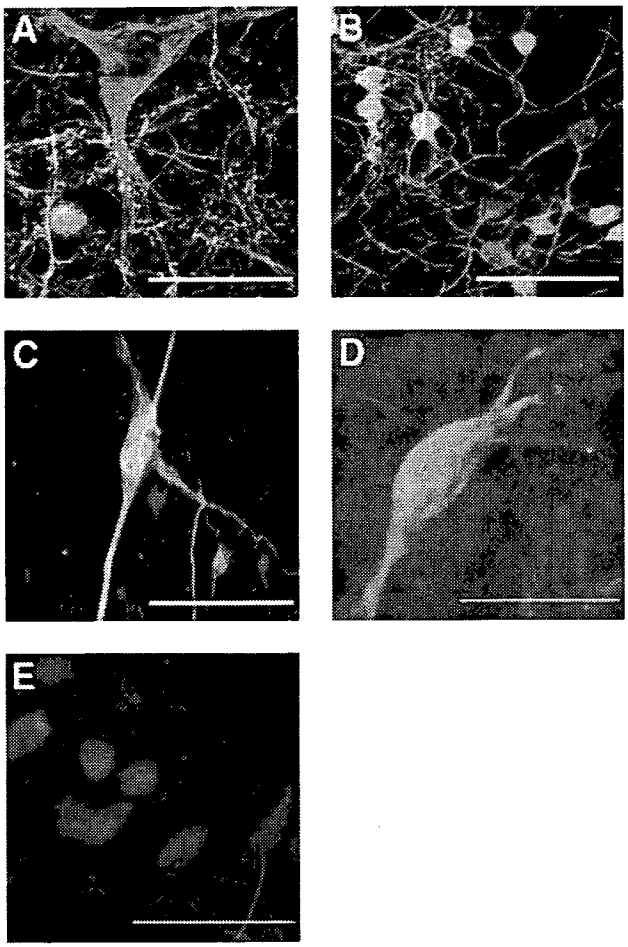

Fig. 8. **A–C:** Calretinin were negative in motor neurons (A; green, calretinin; red, SMI-32; yellow, merge), whereas many small posterior neurons expressed it (B). Relatively large neurons in dorsal horns also expressed calretinin (C). **D, E:** Calbindin D-28K was negative in motor neurons (D; green, SMI-32; red, calbindin D-28K; yellow, merge). There were many positive neurons in posterior horns (E).

rons were more vulnerable to proteasome inhibition than were other kinds of spinal cord neurons in a dissociate culture system (Kikuchi et al., 2002). There was also another report stating that motor neurons were especially vulnerable to proteasome inhibitors and the mutant SOD1-transfected cells fell into proteasomal dysfunction, which leads to motor neuron-specific cell death (Urushitani et al., 2002). On the other hand, nonspecific toxicity was reported with slice cultures of neonatal mice recently (Vlug and Jaarsma, 2004). They used slice cultures applied to proteasome inhibitors and compared the effects between motor neurons and posterior calretinin-positive neurons, as we did in this study. They concluded that both motor neurons and posterior neurons were injured on the same level. However, their study was different from the present study on some points. First, they used clasto-lactacystin β-lacton, which is stronger than the lactacystin we used, and they did not mention the level of proteasome inhibition. Second, they applied the reagents for a week, which was longer than the time used our study. Because proteasome-mediated proteolysis plays a critical role in maintaining homeostasis and regulating signal transduction for survival, excessive inhibition is fatal for any kind of cell. In the present study, a higher concentrate application (more than 100 nM epoxomicin) induced extensive cell death indiscriminately, and longer-term application could also induce indiscriminate cell death, but the present study showed that at an early stage, motor neurons were damaged more easily than posterior neurons.

It is uncertain how motor neurons die under proteasome inhibition. Successful protection by BAPTA-AM must indicate that intracellular Ca^{2+} was the key for motor neuron-specific vulnerability. A major change in intracellular Ca^{2+} could occur in two ways. One is the influx through calcium channels on the cellular membrane and the other is the redistribution of organelles in the cytosol. Mitochondria and endoplasmic reticula (ER) have a large capacity to hold Ca^{2+}. Among these possibilities, we were interested in AMPA receptors, because they are considered to be involved in human sporadic ALS (Kawahara, et al., 2004) and their surface expression is regulated by proteasome-mediated proteolysis of their anchor protein, PSD95 (Colledge et al., 2003). We failed to clarify, however, the benefit of the AMPA receptor blocker CNQX and other agents affecting the influx of Ca^{2+}. It would be useful to examine on the future the redistribution of Ca^{2+} inside a cell.

The neurofilament phosphorylation, the important pathological mark of ALS, is observed in our system. Whether this modification is a primary event or a result

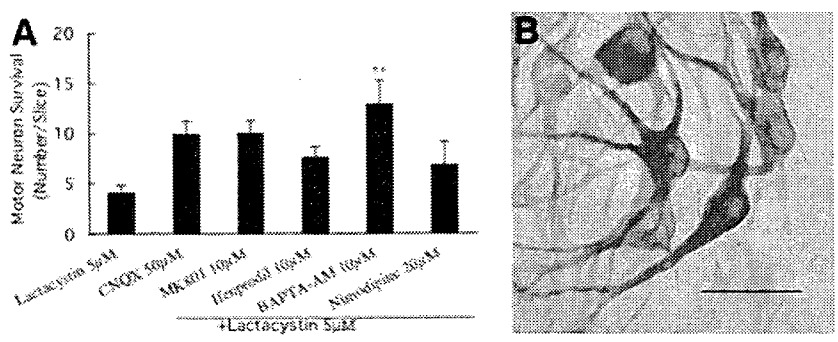

Fig. 9. Cotreated with 5 μM lactacystin and candidates for protection simultaneously for 72 hr. In the BAPTA-AM-treated group motor neuron loss was significantly inhibited (**A**; $^{**}P < 0.01$). **B:** On immunohistochemistry with SMI-32, surviving motor neurons maintained smoothly stretching neurites in a BAPTA-AM-treated slice. Scale bar = 40 μm.

of other primary events remains controversial. Some investigators claim that neurofilaments are working as sinks for excessive kinase, which could be cytotoxic (Nguyen et al., 2003). Because it is supposed to be the early event both in motor neuron degeneration in ALS patients and in our model, searching for the responsible kinase must be meaningful. For example, JNK, a major stress-activated kinase abundantly expressed in the central nervous system, was reported to phosphorylate neurofilaments and to induce apoptotic signals in N2a cells under the proteasome inhibitory condition (Sang et al., 2002). P38/MAPK could also be upregulated by a proteasome inhibitor (Yu et al., 2004) and it can phosphorylate neurofilaments, too (Ackerley et al., 2004). In ALS pathology, JNK/SAPK and p38/MAPK were activated in glial cells and in motor neurons (Migheli et al., 1997). Clarifying the involvement of these pathways in our system might be helpful in understanding the mechanism of the disease.

There is another interesting study about proteasome inhibition using mice spinal cord slice cultures. Puttaparthi et al. (2003) reported reversible accumulation of insoluble proteins and ubiquitinated aggregation in $SOD1^{G93A}$-transgenic mice with lactacystin. In the present study, no visible aggregate was seen in the ubiquitin or SOD1 immunohistochemistry (data not shown), possibly because we used wild-type rats and because the application time was short. Despite the large amount of evidence of aggregate involvement in neuronal death, the meaning remains unclear as to whether it is pathogenic, protective or just a byproduct (Lee et al., 2002; Arrasate et al., 2004). At least, in short-term application, it might not be necessary for motor neuron death.

In various neurodegenerative diseases the proteasome dysfunction is likely a critical mediator involving complex interaction of diverse mechanisms. Aging, oxidative stress, and the existence of mutant proteins could induce proteasome dysfunction (Keller et al., 2000; Urushitani et al., 2002). Proteasome impairment induces mitochondria dysfunction (Sullivan et al., 2004) and oxidative stress (Ding et al., 2004), and causes accumulation of proapoptotic signals (Lang-Rollin et al., 2004). The results of the present study indicate that, among many cascades, proteasome dysfunction is a major factor for motor neurons to decide cellular fate. We hypothesize that one reason for rapid progression of ALS compared to other neurodegenerative disorders is this vulnerability of motor neurons to proteasome dysfunction. We believe our model is useful for examining the motor neuron-specific mechanism in the downstream of proteasome dysfunction, which may be the key mediator in delaying the progression of ALS.

ACKNOWLEDGMENTS

This work was supported by the Research Committee for CNS Degenerative Disease and from Group Research in the Pathogenesis and Pathomechanism of Amyotrophic Lateral Sclerosis, Ministry of Health, Labor, and Welfare of Japan.

REFERENCES

Ackerley S, Grierson AJ, Banner S, Perkinton MS, Brownlees J, Byers HL, Ward M, Thornhill P, Hussain K, Waby JS, Anderton BH, Cooper JD, Dingwall C, Leigh PN, Shaw CE, Miller CC. 2004. p38alpha stress-activated protein kinase phosphorylates neurofilaments and is associated with neurofilament pathology in amyotrophic lateral sclerosis. Mol Cell Neurosci 26:354–364.

Alexianu ME, Ho BK, Mohamed AH, La Bella V, Smith RG, Appel SH. 1994. The role of calcium-binding proteins in selective motoneuron vulnerability in amyotrophic lateral sclerosis. Ann Neurol 36: 846–858.

Arrasate M, Mitra S, Schweitzer ES, Segal MR, Finkbeiner S. 2004. Inclusion body formation reduces levels of mutant huntingtin and the risk of neuronal death. Nature 431:805–810.

Bergold PJ, Casaccia-Bonnefil P. 1997. Preparation of organotypic hippocampal slice cultures using the membrane filter method. Methods Mol Biol 72:15–22.

Bruijn LI, Miller TM, Cleveland DW. 2004. Unraveling the mechanisms involved in motor neuron degeneration in ALS. Annu Rev Neurosci 27:723–749.

Ciechanover A, Brundin P. 2003. The ubiquitin proteasome system in neurodegenerative diseases: sometimes the chicken, sometimes the egg. Neuron 40:427–446.

Colledge M, Snyder EM, Crozier RA, Soderling JA, Jin Y, Langeberg LK, Lu H, Bear MF, Scott JD. 2003. Ubiquitination regulates PSD-95 degradation and AMPA receptor surface expression. Neuron 40:595–607.

Ding Q, Dimayuga E, Markesbery WR, Keller JN. 2004. Proteasome inhibition increases DNA and RNA oxidation in astrocyte and neuron cultures. J Neurochem 91:1121–1218.

Gurney ME, Pu H, Chiu AY, Dal Canto MC, Polchow CY, Alexander DD, Caliendo J, Hentati A, Kwon YW, Deng HX and others. 1994. Motor neuron degeneration in mice that express a human Cu, Zn superoxide dismutase mutation. Science 264:1772–1775.

Kabashi E, Agar JN, Taylor DM, Minotti S, Durham HD. 2004. Focal dysfunction of the proteasome: a pathogenic factor in a mouse model of amyotrophic lateral sclerosis. J Neurochem 89:1325–1335.

Kawahara Y, Ito K, Sun H, Aizawa H, Kanazawa I, Kwak S. 2004. Glutamate receptors: RNA editing and death of motor neurons. Nature 427:801.

Keller JN, Huang FF, Markesbery WR. 2000. Decreased levels of proteasome activity and proteasome expression in aging spinal cord. Neuroscience 98:149–156.

Kikuchi S, Shinpo K, Takeuchi M, Tsuji S, Yabe I, Niino M, Tashiro K. 2002. Effect of geranylgeranylaceton on cellular damage induced by proteasome inhibition in cultured spinal neurons. J Neurosci Res 69: 373–381.

Korhonen L, Lindholm D. 2004. The ubiquitin proteasome system in synaptic and axonal degeneration: a new twist to an old cycle. J Cell Biol 165:27–30.

Lang-Rollin I, Vekrellis K, Wang Q, Rideout HJ, Stefanis L. 2004. Application of proteasomal inhibitors to mouse sympathetic neurons activates the intrinsic apoptotic pathway. J Neurochem 90:1511–1520.

Lee JP, Gerin C, Bindokas VP, Miller R, Ghadge G, Roos RP. 2002. No correlation between aggregates of Cu/Zn superoxide dismutase and cell death in familial amyotrophic lateral sclerosis. J Neurochem 82: 1229–1238.

Migheli A, Piva R, Atzori C, Troost D, Schiffer D. 1997. c-Jun, JNK/SAPK kinases and transcription factor NF-kappa B are selectively activated in astrocytes, but not motor neurons, in amyotrophic lateral sclerosis. J Neuropathol Exp Neurol 56:1314–1322.

Nguyen MD, Boudreau M, Kriz J, Couillard-Despres S, Kaplan DR, Julien JP. 2003. Cell cycle regulators in the neuronal death pathway of amyotrophic lateral sclerosis caused by mutant superoxide dismutase 1. J Neurosci 23:2131–2140.

Puttaparthi K, Wojcik C, Rajendran B, DeMartino GN, Elliott JL, Gitomer WL, Krishnan U, Son M. 2003. Aggregate formation in the spinal cord of mutant SOD1 transgenic mice is reversible and mediated by proteasomes. Disease progression in a transgenic model of familial amyotrophic lateral sclerosis is dependent on both neuronal and non-neuronal zinc binding proteins. J Neurochem 87:851–860.

Reaume AG, Elliott JL, Hoffman EK, Kowall NW, Ferrante RJ, Siwek DF, Wilcox HM, Flood DG, Beal MF, Brown RH Jr, Scott RW, Snider WD. 1996. Motor neurons in Cu/Zn superoxide dismutase-deficient mice develop normally but exhibit enhanced cell death after axonal injury. Nat Genet 13:43–47.

Rosen DR, Siddique T, Patterson D, Figlewicz DA, Sapp P, Hentati A, Donaldson D, Goto J, O'Regan JP, Deng HX, et al. 1993. Mutations in Cu/Zn superoxide dismutase gene are associated with familial amyotrophic lateral sclerosis. Nature 362:59–62.

Rothstein JD, Jin L, Dykes-Hoberg M, Kuncl RW. 1993. Chronic inhibition of glutamate uptake produces a model of slow neurotoxicity. Proc Natl Acad Sci USA 90:6591–6595.

Sang C, Kobayashi Y, Du J, Katsumo M, Adachi H, Doyu M, Sobue G. 2002. c-Jun N-terminal kinase pathway mediates Lactacystin-induced cell death in a neuronal differentiated Neuro2a cell line. Brain Res Mol Brain Res 108:7–17.

Shaw PJ, Ince PG, Falkous G, Mantle D. 1996. Cytoplasmic, lysosomal and matrix protease activities in spinal cord tissue from amyotrophic lateral sclerosis (ALS) and control patients. J Neurol Sci 139(Suppl):71–75.

Stoppini L, Buchs PA, Muller D. 1991. A simple method for organotypic cultures of nervous tissue. J Neurosci Methods 37:173–182.

Sullivan PG, Dragicevic NB, Deng JH, Bai Y, Dimayuga E, Ding Q, Chen Q, Bruce-Keller AJ, Keller JN. 2004. Proteasome inhibition alters neural mitochondrial homeostasis and mitochondria turnover. J Biol Chem 279:20699–20707.

Urushitani M, Kurisu J, Tsukita K, Takahashi R. 2002. Proteasomal inhibition by misfolded mutant superoxide dismutase 1 induces selective motor neuron death in familial amyotrophic lateral sclerosis. J Neurochem 83:1030–1042.

Vanselow BK, Keller BU. 2000. Calcium dynamics and buffering in oculomotor neurones from mouse that are particularly resistant during amyotrophic lateral sclerosis (ALS)-related motoneurone disease. J Physiol 525: 433–445.

Vlug AS, Jaarsma D. 2004. Long term proteasome inhibition does not preferentially afflict motor neurons in organotypical spinal cord cultures. Amyotroph Lateral Scler Other Motor Neuron Disord 5:16–21.

Wood JD, Beaujeux TP, Shaw PJ. 2003. Protein aggregation in motor neurone disorders. Neuropathol Appl Neurobiol 29:529–545.

Yu C, Rahmani M, Dent P, Grant S. 2004. The hierarchical relationship between MAPK signaling and ROS generation in human leukemia cells undergoing apoptosis in response to the proteasome inhibitor Bortezomib. Exp Cell Res 295:555–66.

Available online at www.sciencedirect.com
ScienceDirect
Free Radical Biology & Medicine 42 (2007) 1534–1542
www.elsevier.com/locate/freeradbiomed

Original Contribution

Increased affinity for copper mediated by cysteine 111 in forms of mutant superoxide dismutase 1 linked to amyotrophic lateral sclerosis

Shohei Watanabe [a,1], Seiichi Nagano [a,*,1], James Duce [b], Mahmoud Kiaei [c], Qiao-Xin Li [b], Stephanie M. Tucker [d], Ashutosh Tiwari [e], Robert H. Brown Jr. [f], M. Flint Beal [c], Lawrence J. Hayward [e], Valeria C. Culotta [g], Satoshi Yoshihara [h], Saburo Sakoda [a], Ashley I. Bush [b,d,*]

[a] *Department of Neurology, Osaka University Graduate School of Medicine, Suita, Osaka 565-0871, Japan*
[b] *Oxidation Disorders Laboratory, Mental Health Research Institute of Victoria, and Department of Pathology, University of Melbourne, Parkville, VIC 3052, Australia*
[c] *Department of Neurology and Neuroscience, Weill Medical College of Cornell University, New York, NY 10021, USA*
[d] *Genetics and Aging Research Unit and Department of Psychiatry, Harvard Medical School, Massachusetts General Hospital, Charlestown, MA 02129, USA*
[e] *Department of Neurology, University of Massachusetts Medical School, Worcester, MA 01655, USA*
[f] *Department of Neurology, Massachusetts General Hospital, Charlestown, MA 02129, USA*
[g] *Department of Environmental Health Sciences, Johns Hopkins University Bloomberg School of Public Health, Baltimore, MD 21205, USA*
[h] *Department of Molecular Medicine, Osaka University Graduate School of Medicine, Suita, Osaka 565-0871, Japan*

Received 20 November 2006; revised 4 February 2007; accepted 12 February 2007
Available online 15 February 2007

Abstract

Mutations in Cu,Zn-superoxide dismutase (SOD1) cause familial amyotrophic lateral sclerosis (ALS). It has been proposed that neuronal cell death might occur due to inappropriately increased Cu interaction with mutant SOD1. Using Cu immobilized metal-affinity chromatography (IMAC), we showed that mutant SOD1 (A4V, G85R, and G93A) expressed in transfected COS7 cells, transgenic mouse spinal cord tissue, and transformed yeast possessed higher affinity for Cu than wild-type SOD1. Serine substitution for cysteine at the Cys111 residue in mutant SOD1 abolished the Cu interaction on IMAC. C111S substitution reversed the accelerated degradation of mutant SOD1 in transfected cells, suggesting that the Cys111 residue is critical for the stability of mutant SOD1. Aberrant Cu binding at the Cys111 residue may be a significant factor in altering mutant SOD1 behavior and may explain the benefit of controlling Cu access to mutant SOD1 in models of familial ALS.

Keywords: Amyotrophic lateral sclerosis; Cu,Zn-superoxide dismutase; Copper; Immobilized metal affinity chromatography; Cu chaperone for SOD1; Cysteine; Protein stability; Oxidative stress; Free radicals

Amyotrophic lateral sclerosis (ALS) is a fatal degenerative disease that affects motor neurons. A subset of autosomal dominantly inherited familial ALS (FALS) cases is known to possess mutations of the Cu,Zn-superoxide dismutase (*SOD1*) gene [1]. Transgenic mice that express mutant SOD1, but not wild-type SOD1 nor SOD1 knockout mice, develop motor neuron disease, indicating a toxic gain-of-function of the mutant [2,3]. Although the nature of the mutant SOD1 toxicity has not yet been determined, one hypothesis is that SOD1 mutations lead to oxidative damage associated with an inappropriate redox activity of Cu. Conformational change in mutant SOD1 may

Abbreviations: SOD1, Cu,Zn-superoxide dismutase; ALS, amyotrophic lateral sclerosis; IMAC, immobilized metal affinity chromatography; FALS, familial ALS; CCS, Cu chaperone for SOD1; PCR, polymerase chain reaction; PAGE, polyacrylamide gel electrophoresis; SDS, sodium dodecyl sulfate; PBS, phosphate-buffered saline.

* Corresponding authors. S. Nagano is to be contacted at Department of Neurology, Osaka University Graduate School of Medicine, Suita, Osaka 565-0871, Japan. Fax: +81 6 6879 3579. A.I. Bush, Oxidation Disorders Laboratory, Mental Health Research Institute of Victoria, and Department of Pathology, University of Melbourne, Parkville, VIC 3052, Australia. Fax: +61 3 9387 5061.
E-mail addresses: nagano@neurol.med.osaka-u.ac.jp (S. Nagano), abush@mhri.edu.au (A.I. Bush).
[1] These authors contributed equally to this work.

0891-5849/$ - see front matter © 2007 Elsevier Inc. All rights reserved.
doi:10.1016/j.freeradbiomed.2007.02.004

increase the accessibility of substrates to Cu in the protein to generate reactive oxygen or nitrogen species such as hydroxyl radicals [4] and peroxynitrite [5], which can be inhibited by Cu chelators in cell culture [6,7]. This is the proposed mechanism by which Cu chelators such as D-penicillamine [8], trientine [9,10], and *N*-acetylcysteine [11] rescue mutant SOD1 toxicity in mouse models of FALS. Conversely, genetic ablation of metallothioneins, which sequester excess intracellular metals such as Cu, exacerbated the disease in mutant SOD1 mice [12].

Although SOD1 is a constitutive cuproenzyme, the Cu that may mediate the pathogenic biochemistry does not seem to be the Cu that is coordinated by the active site of mutant SOD1. The evidence for this is the variation in dismutase activity of FALS-linked mutant SOD1 species, which reflects Cu binding at the active site, ranging from nearly 0% to almost 100% [13]. Disease-associated mutation of SOD1 still induces the disease in transgenic mice even when the active copper-binding site is disrupted by multiple substitutions [14–16]. Furthermore, the pathogenic phenotype of mutant SOD1 mice was not rescued by genetic removal of the Cu chaperone for SOD1 (CCS), which incorporates Cu into the buried active site of SOD1 [17]. However, the affinity of the active site of SOD1 for Cu is extremely high, and disrupting the active site does not disrupt all forms of Cu binding to SOD1 [18,19]. Procedures that are likely to remove all but the highest affinity-bound Cu, such as treatment with SDS, were used in appraising Cu incorporation into SOD1 in experiments in which the active site was disrupted or CCS was ablated [14–17]. A pro-oxidative lower affinity interaction between Cu and SOD1 outside the active site has not yet been appraised and therefore cannot yet be excluded from contributing to the FALS phenotype [18,19]. Also, recent data have indicated that CCS overexpression worsens the FALS phenotype in mutant SOD1 mice [20].

There are four Cys residues—Cys6, Cys57, Cys111, and Cys146—in the human SOD subunit. Cys57 and Cys146 form an intramolecular disulfide bond that maintains the protein structure. A FALS-linked SOD1 mutant has been reported to bind Cu at a cysteine residue (Cys111) outside the active site [21]. Cys111 is located as a free cysteine on the protein's surface, near the dimer interface. Substitution of serine for Cys111 was reported to increase the stability of the wild-type SOD1 [22].

To clarify a possible aberrant interaction of mutant SOD1 with Cu outside the active site in the pathogenesis of FALS, and a possible role for Cys111, we studied the affinity for Cu of SOD1 mutants by immobilized metal-affinity chromatography (IMAC). IMAC is a method that can separate proteins depending on their ability to interact with a metal attached to the chromatography matrix [23]. Proteins can be separated by competitive elution with a metal-coordinating agent concentration gradient based on affinity strength. Metal-ligating residues such as cysteine, especially at the solvent-facing regions, determine the affinity of proteins for the metal [24,25]. The technique has been used to investigate the metal affinity of native proteins, including human SOD1 [26,27], and also to identify metal binding sites within proteins, e.g., the Cu and Zn binding sites on the β-amyloid precursor protein involved in Alzheimer disease [28,29].

We found that forms of mutant SOD1 had higher affinity for Cu than wild-type SOD1 and that mutant SOD1 with the C111S substitution markedly attenuated Cu affinity and increased protein stability. This may account for the evidence supporting an interaction with Cu as playing a role in the pathogenesis of FALS and implicates Cys111 as a key site for this interaction.

Experimental procedures

Expression plasmids

Expression vectors of human wild-type and mutant (A4V, G85R, and G93A) SOD1 cDNAs were constructed using the polymerase chain reaction (PCR) on the *Eco*RI and *Eco*RV sites of the pTracer-CMV2 plasmid (Invitrogen, Carlsbad, CA, USA). The sequences of the primers for PCR were 5′-GCCGAATTCCTAGCGAGTTATGGCGACGAA-3′ (*Eco*RI) and 5′-GCCGATATCAAGGGAATGTTTATTGGGCGA-3′ (*Eco*RV). Using the mutant SOD1 vectors as templates, mutants with C57S or C111S substitution were obtained by site-directed mutagenesis using *PfuTurbo* DNA polymerase and *Dpn*I endonuclease (Stratagene, La Jolla, CA, USA) in accordance with the procedure of the QuickChange site-directed mutagenesis kit. The entire nucleotide sequence of these SOD1 cDNAs was confirmed by the ABI Prism 310 genetic analyzer (Applied Biosystems, Foster City, CA, USA).

Cell culture and transfection

COS7 cells were cultured in Dulbecco's modified Eagle's medium with 10% fetal bovine serum and antibiotics. COS7 cells were seeded at 1.5×10^5 cells per dish on 60 × 15-mm cell culture dishes, cultured, and then transfected with 2.0 μg of the vector carrying the wild-type or mutant SOD1. Transfections were performed using the FuGENE6 transfection reagent (Roche, Indianapolis, IN, USA) according to the manufacturer's instructions. Forty-eight hours after transfection, the cultured cells were homogenized using glass beads of size 420–500 μm (Polysciences, Warrington, PA, USA) in 500 μl of buffer A (50 mM Tris, 1 M NaCl, pH 7.4) containing 0.1% Triton X and protease inhibitor cocktail without metal chelators (Sigma, St. Louis, MO, USA). After the cell lysates were centrifuged (20,400*g*, 5 min), the supernatant was collected and applied to the IMAC column. The supernatant was also directly analyzed by polyacrylamide gel electrophoresis (PAGE), as described later.

For cycloheximide assays, COS7 cells were seeded at 4×10^4 cells per well on six-well cell culture clusters and cultured; they were then transfected with 1.0 μg of the vector carrying the wild-type or mutant SOD1.

Transgenic mice

All protocols were conducted within NIH guidelines for animal research and were approved by the Institutional Animal Care and Use Committee. Transgenic mice that express the human G85R [3] or G93A [2] *SOD1* gene, both of which cause

the ALS phenotype, were maintained as hemizygotes and euthanized at the symptomatic age (≈9 months for G85R and ≈8 months for G93A mice). The G93A transgenic mice with a delayed phenotype (TgN[SOD1-G93A]1Gurdl) were originally obtained from The Jackson Laboratory (Bar Harbor, ME, USA) and maintained by breeding hemizygous carriers to a C57BL/6 mouse strain. The delayed phenotype compared with the originally published phenotype is due to a reduction in transgene copy number. Human wild-type *SOD1* transgenic mice (N1029) [2] were used as the controls. All transgenic progeny were identified by PCR of tail genomic DNA as described previously [2]. Animals were perfused and spinal cords from the mice were dissected, weighed, and then homogenized with 5× wet weight (1 ml/g) of buffer A containing protease inhibitor cocktail. After the centrifugation of the homogenate (100,000*g*, 30 min), the supernatant was kept for IMAC.

Yeast strains and culture conditions

The *Saccharomyces cerevisiae* strains KS107 (*sod1*Δ::*TRP1*) and PS131 (*ccs1*Δ::*TRP1*), which lack endogenous yeast *SOD1* and *ccs1* genes, respectively, were derived from the parental strain EG103 (*MATα leu2–3, 112 his3*Δ*1 trp1–289 ura3–52*) [30]. Plasmid pLC1 (2μ *URA3*) expresses human wild-type SOD1 under the control of *S. cerevisiae PGK1*, as described [31]. The human SOD1 mutant A4V or G85R was obtained by site-directed mutagenesis of pLC1. All yeast strains were grown in (−)URA synthetic dextrose liquid medium aerobically at 30°C. The cell pellets from 100 ml of overnight culture were homogenized with glass beads in 500 μl buffer A containing 0.1% Triton X and protease inhibitor cocktail. After the centrifugation of the homogenate (20,400*g*, 5 min), the supernatant was kept for IMAC.

Polyacrylamide gel electrophoresis and Western blot analysis

Samples were electrophoresed on 4–20% Tris–glycine polyacrylamide gradient gels (Invitrogen) containing SDS in running buffer and loading dye with 5% 2-mercaptoethanol (SDS–PAGE). PAGE samples were electrotransferred to polyvinylidene fluoride membrane, which was then blocked overnight at 4°C with 10% nonfat milk and then incubated for 1 h at room temperature with primary antibody in Tris-buffered saline containing 0.1% Tween 20. Sheep anti-human SOD1 antibody (Calbiochem, Darmstadt, Germany) that cross-reacts with mouse SOD1 was used in most experiments, whereas rabbit anti-human SOD1-specific antibody (Chemicon, Temecula, CA, USA) [32] was used for blots of the samples from the transgenic mice, because the expression level of human SOD1 in the mice is relatively low compared with that of endogenous mouse SOD1. After incubation of the membranes for 1 h at room temperature with corresponding horseradish peroxidase-conjugated secondary antibody, the protein bands were visualized using the SuperSignal West Pico chemiluminescent (Pierce, Rockford, IL, USA) or the ECL Western blotting detection (Amersham, Uppsala, Sweden) system. For the elution profile of SOD1, the densities of the protein bands were measured on the membranes using NIH Image 1.62 (National Institutes of Health, Bethesda, MD, USA).

Immobilized metal-affinity chromatography

Chelating Sepharose Fast Flow (400-μl bed volume; Amersham) was packed into disposable 2-ml polystyrene columns (Pierce); the resin was presaturated with either $CuCl_2$ or $ZnCl_2$ at 20 mM and equilibrated with buffer A. The extracts of cells or tissue (500 μl, ≈0.5 mg for cells and ≈2.5 mg for tissue) were applied to the column, and the column was washed with buffer A (500 μl). After additional washing with buffer A (3 ml), the proteins were eluted using a stepwise imidazole gradient (0–100 mM, each fraction was 500 μl) in buffer A. Finally, the column was stripped of all bound Cu with 50 mM EDTA. In some experiments the sample was loaded, the column washed, and the column developed with a 30 mM imidazole step followed by a 50 mM EDTA step (500 μl each). The eluted SOD1 was analyzed in each fraction (normalized for elution volume) by immunoblotting.

For comparison of the elution profiles of SOD1 from the IMAC column, samples were normalized for total proteins and brought to the same protein concentration before being loaded onto the column. Protein concentrations of starting material, flowthrough, and elution fractions were measured by BCA assay (Pierce). The starting sample and each IMAC fraction were analyzed by SDS–PAGE and immunoblotted.

Cycloheximide assays

This protocol was based on a previously reported method [33]. Forty-eight hours after transfection, the cultured COS7 cells were washed with phosphate-buffered saline (PBS) and treated for the indicated times with serum-free medium containing 1 mg/ml cycloheximide (Sigma). The cells were then homogenized with glass beads in 200 μl buffer B (0.1% SDS and protease inhibitor cocktail in PBS). After the cell lysates were centrifuged (20,400*g*, 5 min), the supernatant was collected. This supernatant was subjected to Western blot analysis with sheep anti-human SOD1 and mouse anti-β-actin (Sigma) antibody.

Results

To study the affinity of mutant and wild-type SOD1 for Cu, we applied extracts of transfected COS7 cells to Cu–IMAC. The expression level of human SOD1 in each line was similar. The Cu–IMAC column was developed with a concentration gradient of imidazole (a relatively low-affinity Cu-coordinating agent) followed by an EDTA solution (a high-affinity Cu chelator). Fig. 1A plots the typical elution profile for both total protein and SOD1 (assayed by densitometry of Western blot) from cells expressing wild-type human SOD1 or G85R mutant SOD1. The total protein elution profile was indistinguishable. However, ≈50% of the G85R mutant SOD1 eluted at imidazole concentrations above 30 mM, whereas most of the wild-type SOD1 had eluted by 30 mM imidazole, and almost none

exhibited this higher Cu-affinity interaction. The total protein elution profile was similar in all of the cell lines we studied.

Figs. 1B–1D show SOD1 Western blots of the Cu–IMAC fraction from cells expressing wild-type human SOD1, mutant SOD1, and mutant SOD1 with C57S substitution or with C111S substitution. The elution profiles of the three pathogenic SOD1 mutants examined were all similarly shifted to increased Cu affinity relative to the normal human SOD1 profile. Wild-type SOD1 was almost completely eluted by 20 mM imidazole. In contrast, the pathogenic mutants required much higher imidazole concentrations (up to 50 mM) to be fully eluted from the Cu–IMAC, implying a gain in Cu affinity. The C57S substitution did not inhibit the increased Cu affinity of the three mutant forms of SOD1, but seemed to diminish the lower affinity Cu interactions (Figs. 1B–1D). In contrast, the C111S substitution dramatically disrupted Cu interaction in all three pathogenic mutants, causing ≈90% of the SOD1 to elute at imidazole concentrations ≤20 mM. The proportions of mutant SOD1 exhibiting high-affinity Cu interactions were markedly greater than wild-type SOD1 when expressed in these cells (Fig. 1E). The proportions of high-affinity Cu interaction became equivalent between wild-type and mutant SOD1 when the mutant was substituted with C111S (Fig. 1E). These data indicate that increased Cu affinity is a feature in common for the three mutant forms of SOD1 tested and is mediated by the Cys111 residue.

Because cysteine may also coordinate Zn^{2+}, we repeated the IMAC with Zn^{2+} for both wild-type and mutant SOD1 expressed in COS7 cells. The interaction with Zn was much weaker than with Cu for either wild-type or mutant SOD1, with almost no binding to the Zn on the column (data not shown). This indicates that SOD1 principally interacts with Cu rather than Zn in this system.

To determine whether the increase in Cu affinity of mutant SOD1 occurs in vivo, we analyzed spinal cord tissue from

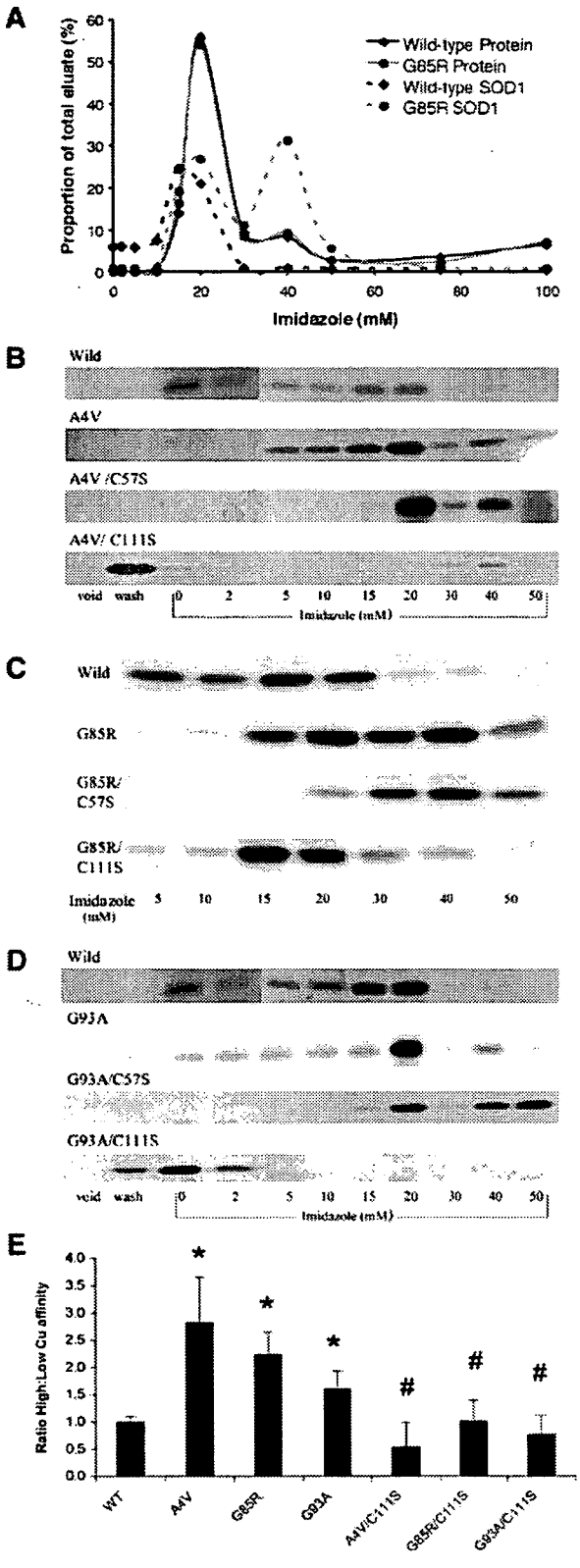

Fig. 1. Cu–IMAC elution profiles of human SOD1 from extracts of transfected COS7 cells. Soluble proteins from the lysates of COS7 cells expressing human wild-type or mutant (A4V, G85R, and G93A) SOD1, mutant SOD1 with C57S substitution, or mutant SOD1 with C111S substitution were applied to Cu–IMAC and eluted with increasing concentrations of imidazole. The eluted fractions were measured for total protein levels and human SOD1. Cu–IMAC eluates from wild-type SOD1 cells were used as reference profiles for comparison against the mutants in every blot series. (A) Protein and SOD1 elution profiles from extracts of COS7 cells transfected with normal human SOD1 ("Wild-type") or G85R mutant SOD1. The graph shows the amounts of eluted proteins or SOD1 per fraction, as a percentage of the total eluted proteins or SOD1, across an imidazole gradient. (B) Western blots typical of SOD1 levels in Cu–IMAC fractions from cells transfected with A4V, A4V/C57S, and A4V/C111S SOD1. (C) SOD1 Western blots in Cu–IMAC fractions from cells transfected with G85R, G85R/C57S, and G85R/C111S SOD1. (D) SOD1 Western blots in Cu–IMAC fractions from cells transfected with G93A, G93A/C57S, and G93A/C111S SOD1. Void, starting material that was not bound to the column; wash, the fraction obtained after the washing step with 500 µl buffer A (50 mM Tris, 1 M NaCl, pH 7.4). (E) Proportion of higher Cu-affinity mutant compared to wild-type human SOD1. Soluble proteins from cell lysates were fractionated by limited Cu–IMAC to generate 30 mM imidazole (low Cu affinity) and 50 mM EDTA (high Cu affinity) eluates. The relative amounts of SOD1 in these fractions were calculated by densitometry of immunoblots. The graph indicates the amount of human SOD1 eluting with high Cu affinity expressed as a proportion of SOD1 eluting with low Cu affinity. The ratio for each mutant was standardized to that for wild-type SOD1 (set at 1.0) for comparison. Data are means±SD from four (wild type, WT) or three (the others) independent experiments. $*p < 0.05$ compared to wild-type SOD1, $\#p < 0.05$ compared to the respective mutant without C111S substitution by two-tailed t test.

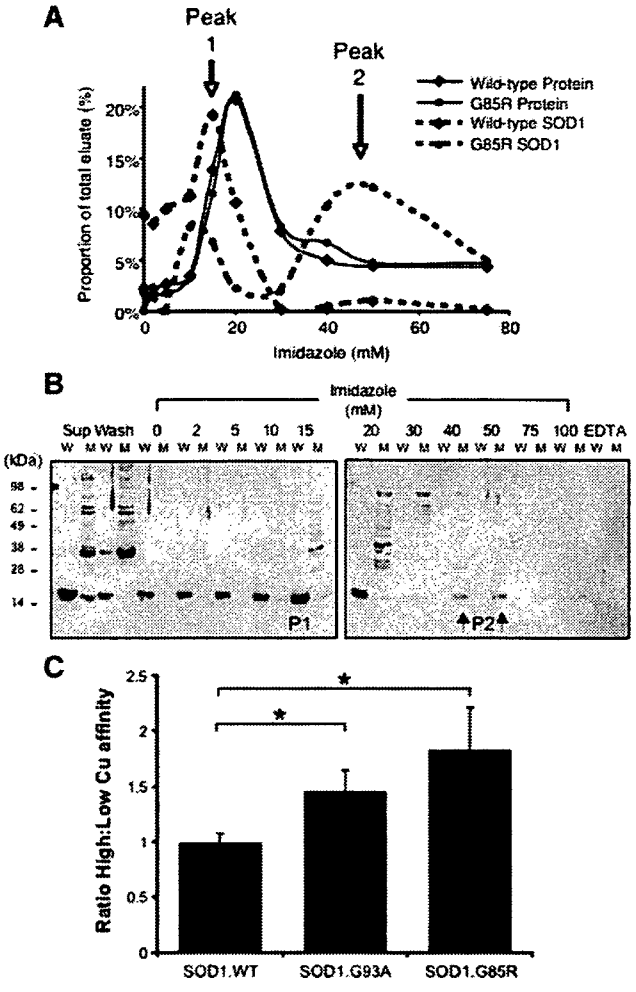

Fig. 2. Cu–IMAC elution profiles of human SOD1 from spinal cord extracts of transgenic mice. (A) Protein and SOD1 elution profiles from spinal cords (soluble fraction) of 9-month old human wild-type and G85R mutant SOD1 transgenic mice. The graph shows the amounts of eluted proteins or SOD1 per fraction, as a percentage of the total eluted proteins or SOD1, across an imidazole gradient. The lower (peak 1) and higher (peak 2) Cu-affinity SOD1 elution peaks are shown by arrows. These results are typical of $N = 3$ experiments. (B) Western blots of the elution of human wild-type (W) and G85R (M) SOD1. Eluted fractions as indicated were electrophoresed and immunoblotted for human-SOD1-specific antibody. For this experiment, we applied 1/10 the amount of the original fractions from wild-type SOD1 mice because SOD1 expression is much greater than that of G85R SOD1 in the mice. Sup, starting material; Wash, starting material unbound to the column; EDTA, column was stripped with 50 mM EDTA and eluted protein assayed for SOD1. Arrows indicate mutant SOD1 bands eluting with a higher affinity for Cu than wild-type SOD1. P1 and P2 correspond to peak 1 and peak 2 in A, respectively. (C) Proportion of higher Cu affinity mutant compared to wild-type human SOD1. Soluble proteins from spinal cord tissue homogenates ($N = 4$ each) of human wild-type (WT), symptomatic G85R (9 months of age), and G93A (8 months of age) SOD1 transgenic mice were fractionated by limited Cu–IMAC to generate just 30 mM imidazole (low Cu affinity) and 50 mM EDTA (high Cu affinity) eluates. The relative amounts of SOD1 in these fractions were calculated by densitometry of anti-human-specific SOD1 immunoblots. The graph indicates the ratio of human SOD1 eluting with high Cu affinity expressed as a proportion of the amount of SOD1 eluting with low Cu affinity. The ratio for each mutant was standardized to that of wild-type SOD1 for comparison. Data are means ± SEM, $N = 4$ samples, each assayed in duplicate. $^*p < 0.05$ by two-tailed t test.

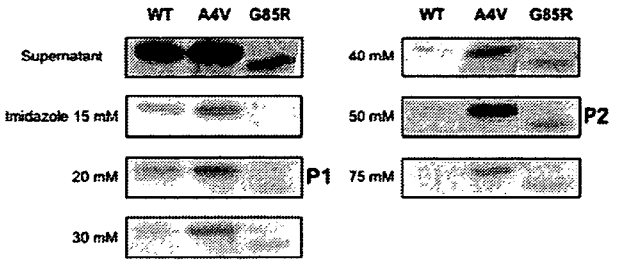

Fig. 3. Cu–IMAC elution profiles of human SOD1 from extracts of transformed *CCS1* Δ yeast. Soluble proteins from cell lysates (starting material, "Supernatant") of the PS131 yeast strain expressing wild-type (WT), A4V, or G85R SOD1 were fractionated by Cu–IMAC. Fractions were immunoblotted using SOD1 antibody. The first (P1) and second (P2) SOD1 elution peaks are indicated. Results are each typical of $N = 3$ experiments.

transgenic mice by Cu–IMAC. Typical of all transgenic tissue we examined, and similar to the profile of SOD1 expressed in COS7 cells (Fig. 1A), there was no difference in the total protein distribution within the imidazole gradient elution fractions between N1029 and G85R transgenic spinal cord extract (Fig. 2A). Wild-type human SOD1 eluted with one Cu-binding peak with slightly lower affinity than most of the other proteins that bind to Cu (peak 1 ≈15 mM imidazole, Figs. 2A and 2B). However, as was observed in cell culture (Fig. 1), G85R SOD1 exhibited not only this lower affinity Cu interaction, but also a higher affinity peak that indicated enrichment of the mutant compared with the other proteins (peak 2 ≈50 mM imidazole, Figs. 2A and 2B). The increase in Cu affinity of mutant SOD1 was also observed in G93A transgenic spinal cord tissue (Fig. 2C) relative to normal human SOD1 expressed in transgenic N1029 spinal cord (Fig. 2C).

To characterize mutant SOD1 interaction with Cu in a nonmammalian system, we studied the elution profiles of supernatants extracted from yeast expressing human wild-type and mutant SOD1 by Cu–IMAC. We utilized a *ccs1*-deficient yeast strain [30] to exclude the possible binding of CCS to SOD1 as mediating the Cu–IMAC interaction. Wild-type human SOD1 expressed in the yeast eluted with a single low-affinity Cu-binding peak at 15–20 mM imidazole (P1, Fig. 3), a Cu affinity similar to that of wild-type human SOD1 expressed in cells or the spinal cords of mice (Figs. 1 and 2). Also similar to the Cu affinity of SOD1 expressed in cells (Fig. 1), the A4V mutant manifested a second, higher affinity Cu-binding property (P2) in addition to a minor peak (P1) at the same position as that of wild-type SOD1 (Fig. 3). For G85R expressed in yeast, the lower affinity Cu binding was not detectable and only the higher affinity Cu binding (P2) was identified (Fig. 3), indicating that the increased Cu-affinity species represent a substantial proportion of total mutant SOD1. These data confirm that the increase in the affinity for Cu in mutant SOD1 is independent of CCS. We also examined the elution patterns of human SOD1 expressed in a yeast strain that lacks the endogenous yeast *sod1* gene and detected no difference from the pattern of SOD1 elution obtained with the *ccs1*-deficient strain (data not shown). This means that endogenous wild-type SOD1 has no influence on the elution

of mutant SOD1 by an interaction such as heterodimer formation.

To examine the effect of C111S substitution on the stability of the mutant SOD1 protein, we analyzed the degradation of SOD1 in transfected cells in which protein translation had been inhibited with cycloheximide [34]. The transfected COS7 cells were treated with cycloheximide and harvested after 6 and 12 h whereupon cellular SOD1 turnover was analyzed by Western blotting using the anti-β-actin antibody as a loading control (Fig. 4). The levels of A4V, G85R, and G93A SOD1 proteins decreased more rapidly than the levels of wild-type SOD1 and were significantly lower after 12 h treatment with cycloheximide (Fig. 4B). Mutant SOD1 with C57S substitution degraded at a rate that was indistinguishable from that of the mutant without the substitution (Fig. 4A). However, after 12 h incubation with cycloheximide, the mutants with C111S substitution were significantly more stable (Figs. 4A and 4B),

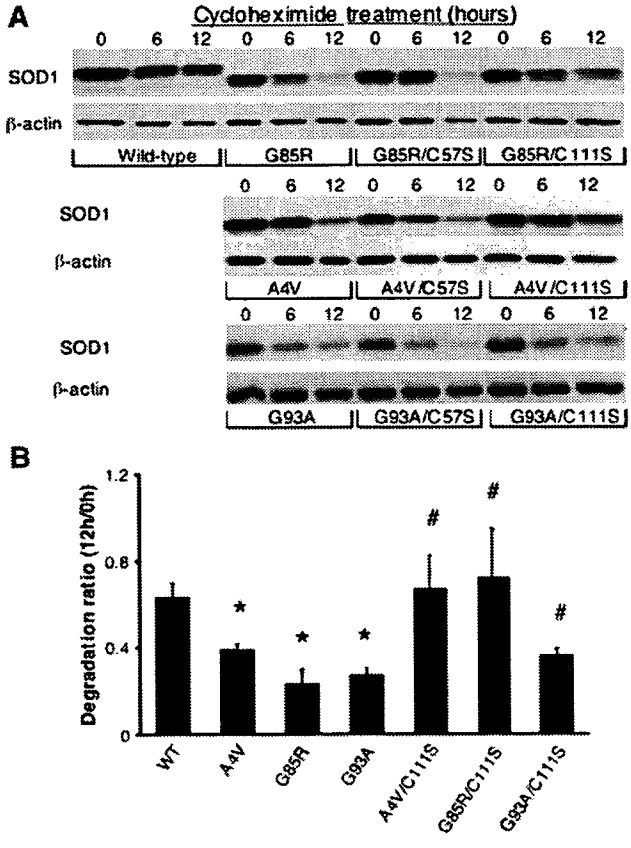

Fig. 4. Stability of wild-type and mutant SOD1 analyzed by cycloheximide inhibition of protein synthesis. The COS7 cells were transfected with wild-type, mutant (A4V, G85R, and G93A), mutant with C57S, or mutant with C111S human SOD1, and after 48 h, they were treated with cycloheximide (1 mg/ml) for different times (0, 6, and 12 h). (A) Typical SOD1 Western blots of soluble fractions of cell lysates from each type of transfected cell preparation. β-Actin loading controls are shown. (B) Amounts of SOD1 protein remaining in transfected cells 12 h after cycloheximide addition. The amount of SOD1 at each time point was calculated by densitometry using SOD1 immunoblots. The graph indicates the ratio of SOD1 remaining after 12 h of cycloheximide treatment versus the amount of SOD1 at 0 h (starting levels) in each line. Data are means ± SD from three independent experiments. $*p < 0.01$ compared to wild-type SOD1, $\#p < 0.05$ compared to the respective mutant without C111S substitution by two-tailed t test.

approaching wild-type levels. These results indicate that Cys111 is the critical residue for the concomitant instability of mutant SOD1, as well as its increased Cu affinity.

Discussion

In this study, we used Cu–IMAC to demonstrate an increase in the affinity of mutant SOD1 for Cu (Figs. 1, 2, and 3) and a critical role for the Cys111 residue (Fig. 1) in this interaction. Cysteine, histidine, glutamate, aspartate, and tyrosine are residues that coordinate binding to the immobilized metal in IMAC. SOD1 binding to Cu on IMAC resin is unlikely to be mediated by the intact active site coordinating residues because the affinity of the active site for Cu (K_d=femtomolar) [35] would be too high to be competed for by imidazole, a low-affinity metal-coordinating agent, at this concentration. The interaction of wild-type SOD1 with Cu we observed (Figs. 1, 2, and 3) is relatively low affinity and probably mediated by solvent-facing residues. The increased Cu affinity of G85R SOD1 (Figs. 1A, 1C, 2, and 3) is an important observation because these mutants do not efficiently incorporate Cu [13], and therefore the immobilized Cu is likely to be interacting with SOD1 residues outside the active site, on a solvent-facing surface.

We hypothesized that Cys111 could be a candidate site in human SOD1 that could mediate the enhanced coordination of the immobilized Cu. Previous in vitro studies indicated that Cu abnormally binds to Cys111 in H46R mutant SOD1 [21]. The importance of Cys111 for the stability of SOD1 was underscored by findings that C111S substitution in wild-type SOD1 increased resistance to heat inactivation and the conformational stability of the protein [22]. Indeed, bovine wild-type SOD1, which lacks Cys at position 111, is reported to be more stable than human SOD1 [22]. In agreement with those previous findings, we found that Cys111 played a pivotal role in the increased Cu affinity and stability of mutant SOD1. C111S substitution in mutant SOD1 (A4V, G85R, and G93A) negated the increase in Cu binding (Fig. 1) while stabilizing the mutant (Fig. 4). This is important because previous reports have indicated that the decreased stability of mutant SOD1 could be related to its toxicity [36] and correlates with disease progression [37].

To examine whether other cysteine residues of mutant SOD1 play the same role as Cys111, we introduced C57S substitution into the protein. In contrast to the effects of Cys111 substitution, C57S substitution increased Cu binding (Figs. 1B–1D) and did not rescue mutant instability (Fig. 4A). C57S substitution prevents the disulfide bond between Cys57 and Cys146. In general, increasing the number of disulfide bonds in a protein enhances stability by reducing the conformational entropy of the unfolded protein [38]. Human SOD1 protein is reported to be unstable without the intrasubunit disulfide bond [39]. Although the function of the disulfide bond in SOD1 is not fully elucidated [40], it could be related to either the dimerization of SOD1 or the metal binding process at the active site or both [41]. Thus, mutant SOD1 with C57S may become conformationally further destabilized, exposing Cu-interaction sites such as Cys111 to enhance Cu affinity of the protein.

The mechanism by which Cys111 mediates the increased Cu affinity of mutant SOD1 is not yet clear. One possibility is that a cellular factor selectively modifies Cys111 in mutant SOD1. The factor may be a Cu^{2+}-coordinating protein or moiety such as a glutathione or carbonyl group [42–44]. Cys111 is reported to be a target of posttranslational modifications, such as glutathionylation [45]. These interactions may be dissociated by SDS or may be small in molecular weight, because a shift of the SOD1 band on SDS–PAGE was not discernable. Data from ion-exchange chromatography of erythrocyte extracts from FALS patients with SOD1 mutations and controls [46] support this possibility: the samples from FALS patients exhibited abnormal Cu-containing fractions that separated from fractions containing SOD1 activity. Our data excluded CCS as the Cu-binding interacting protein because, even in *ccs1*-deficient yeast, mutant SOD1 exhibited higher Cu affinity (Fig. 3). The interacting factor at Cys111 may alternatively induce a conformational change in mutant SOD1 that exposes buried Cu^{2+}-coordinating residues, such as the Zn^{2+} binding site or histidine 110 adjacent to Cys111, which is conserved in mammalian species. Both are potentially Cu^{2+}-coordinating sites. Even when the active Cu site of SOD1 is disrupted in the quadruple mutant transgenic mice (H46R/H48Q/H63G/H120G) [16], the Zn binding site retains an aspartate plus two histidines, which is a powerful metal binding motif. A third possibility is that Cys111 in mutants is merely more stable in the reduced (–SH) state and acts, in concert with His110, to bind Cu directly, which has been demonstrated in H46R mutant SOD1 [21]. Wild-type SOD1 may be more likely than mutant SOD1 to become oxidized, or to form mixed disulfide adducts, at Cys111, so disabling this residue as a Cu ligand.

Our findings also indicate that only a fraction of mutant SOD1 in the cell develops increased Cu affinity. This is congruent with evidence that the disease phenotype is mediated by only a fraction of the total expressed mutant SOD1 [47]. We hypothesize that this subpopulation of mutant SOD1 may mediate a toxic interaction with Cu^{2+} that contributes to the pathogenesis of FALS. Although previous evidence had excluded active-site Cu interaction as mediating toxicity, our current data indicate that a non-dismutase Cu-binding site, Cys111, could account for the evidence that aberrant Cu interaction with mutant SOD1 plays a role in FALS pathogenesis. It is notable that even in the absence of CCS, SOD1 still retains 15–20% Cu-mediated activity [17]. It has been estimated that this residual copper binding still represents a substantial concentration of intracellular Cu (10 μM) in SOD1-overexpressing transgenic mice [18], demonstrating the ability of SOD1 to recruit Cu in vivo even in the absence of the active-site insertion mechanism.

Incorrectly coordinated Cu^{2+} is highly redox active and therefore potentially toxic. An increased Cu^{2+} interaction with mutant SOD1 may foster pro-oxidant activities, including the generation of reactive oxygen [4,6] or nitrogen species [5,35]. Cu-mediated reactions may also oxidize mutant SOD1 itself to become pathogenic by causing misfolding and aggregation of the protein [48]. By analogy, ceruloplasmin, another abundant antioxidant cuproenzyme (ferroxidase), also abnormally binds chelatable Cu on a surface outside its active Cu binding sites to generate abnormal pro-oxidative activity [49]. This may be the mechanistic explanation for the evidence of cellular Cu playing a role in the toxicity of mutant SOD1.

The degree of increase in Cu affinity that was caused by each FALS-linked SOD1 mutation we studied was variable between mutations, but was reasonably consistent between expression systems. For example, G93A seemed to cause less of an increase in Cu affinity than G85R in both cell culture (Fig. 1E) and transgenic mouse tissue (Fig. 2C). However, our survey of mutations was limited, and further studies will be needed to confirm that the relative gain in Cu affinity consistently varies according to the particular SOD1 mutation. It will also be important to determine whether the degree of gain in Cu affinity correlates with the severity of the clinical phenotype.

The current data support consideration of cellular Cu interactions with mutant SOD1 as a potential mediator of neurodegeneration in the pathogenesis of FALS and the possibility of interdicting the reaction at the Cys111 residue as a potential pharmacological target.

Acknowledgments

This work was supported by grants from the Amyotrophic Lateral Sclerosis Association (to A.I.B., M.F.B., and M.K.), funds from the Australian Research Council (Federation Fellowship to A.I.B.), the National Health and Medical Research Council of Australia (to A.I.B.), the National Institutes of Health (GM 50016 to V.C.C.), and the Ministry of Education, Culture, Science, and Technology of Japan (to S.N.).

References

[1] Rosen, D. R.; Siddique, T.; Patterson, D.; Figlewicz, D. A.; Sapp, P.; Hentati, A.; Donaldson, D.; Goto, J.; O'Regan, J. P.; Deng, H. X.; Rahmani, Z.; Krizus, A.; McKenna-Yasek, D.; Cayabyab, A.; Gaston, S. M.; Berger, R.; Tanzi, R. E.; Halperin, J. J.; Herzfeldt, B.; Van den Bergh, R.; Hung, W. Y.; Bird, T.; Deng, G.; Mulder, D. W.; Smyth, C.; Laing, N. G.; Soriano, E.; Pericak-Vance, M. A.; Haines, J.; Rouleau, G. A.; Gusella, J. S.; Horvitz, H. R.; Brown, R. H. J. Mutations in Cu/Zn superoxide dismutase gene are associated with familial amyotrophic lateral sclerosis [published erratum appears in Nature 1993 364:362][see comments]. *Nature* **362**:59–62; 1993.

[2] Gurney, M. E.; Pu, H.; Chiu, A. Y.; Dal Canto, M. C.; Polchow, C. Y.; Alexander, D. D.; Caliendo, J.; Hentati, A.; Kwon, Y. W.; Deng, H. X.; Chen, W.; Zhai, P.; Sufit, R. L.; Siddique, T. Motor neuron degeneration in mice that express a human Cu,Zn superoxide dismutase mutation [see comments] [published erratum appears in *Science* 1995 **269**:149]. *Science* **264**:1772–1775; 1994.

[3] Bruijn, L. I.; Becher, M. W.; Lee, M. K.; Anderson, K. L.; Jenkins, N. A.; Copeland, N. G.; Sisodia, S. S.; Rothstein, J. D.; Borchelt, D. R.; Price, D. L.; Cleveland, D. W. ALS-linked SOD1 mutant G85R mediates damage to astrocytes and promotes rapidly progressive disease with SOD1-containing inclusions. *Neuron* **18**:327–338; 1997.

[4] Yim, M. B.; Kang, J. H.; Yim, H. S.; Kwak, H. S.; Chock, P. B.; Stadtman, E. R. A gain-of-function of an amyotrophic lateral sclerosis-associated Cu, Zn-superoxide dismutase mutant: an enhancement of free radical formation due to a decrease in Km for hydrogen peroxide. *Proc. Natl. Acad. Sci. USA* **93**:5709–5714; 1996.

[5] Beckman, J. S.; Carson, M.; Smith, C. D.; Koppenol, W. H. ALS, SOD and peroxynitrite [letter]. *Nature* **364**:584; 1993.

[6] Wiedau Pazos, M.; Goto, J. J.; Rabizadeh, S.; Gralla, E. B.; Roe, J. A.; Lee, M. K.; Valentine, J. S.; Bredesen, D. E. Altered reactivity of superoxide dismutase in familial amyotrophic lateral sclerosis [see comments]. *Science* **271**:515–518; 1996.

[7] Ghadge, G. D.; Lee, J. P.; Bindokas, V. P.; Jordan, J.; Ma, L.; Miller, R. J.; Roos, R. P. Mutant superoxide dismutase-1-linked familial amyotrophic lateral sclerosis: molecular mechanisms of neuronal death and protection. *J. Neurosci.* **17**:8756–8766; 1997.

[8] Hottinger, A. F.; Fine, E. G.; Gurney, M. E.; Zurn, A. D.; Aebischer, P. The copper chelator d-penicillamine delays onset of disease and extends survival in a transgenic mouse model of familial amyotrophic lateral sclerosis. *Eur. J. Neurosci.* **9**:1548–1551; 1997.

[9] Nagano, S.; Ogawa, Y.; Yanagihara, T.; Sakoda, S. Benefit of a combined treatment with trientine and ascorbate in familial amyotrophic lateral sclerosis model mice. *Neurosci. Lett.* **265**:159–162; 1999.

[10] Nagano, S.; Fujii, Y.; Yamamoto, T.; Taniyama, M.; Fukada, K.; Yanagihara, T.; Sakoda, S. The efficacy of trientine or ascorbate alone compared to that of the combined treatment with these two agents in familial amyotrophic lateral sclerosis model mice. *Exp. Neurol.* **179**: 176–180; 2003.

[11] Andreassen, O. A.; Dedeoglu, A.; Klivenyi, P.; Beal, M. F.; Bush, A. I. *N*-Acetyl-L-cysteine improves survival and preserves motor performance in an animal model of familial amyotrophic lateral sclerosis. *Neuroreport* **11**:2491–2493; 2000.

[12] Nagano, S.; Satoh, M.; Sumi, H.; Fujimura, H.; Tohyama, C.; Yanagihara, T.; Sakoda, S. Reduction of metallothioneins promotes the disease expression of familial amyotrophic lateral sclerosis mice in a dose-dependent manner. *Eur. J. Neurosci.* **13**:1363–1370; 2001.

[13] Hayward, L. J.; Rodriguez, J. A.; Kim, J. W.; Tiwari, A.; Goto, J. J.; Cabelli, D. E.; Valentine, J. S.; Brown Jr., R. H. Decreased metallation and activity in subsets of mutant superoxide dismutases associated with familial amyotrophic lateral sclerosis. *J. Biol. Chem.* **277**:15923–15931; 2002.

[14] Wang, J.; Xu, G.; Gonzales, V.; Coonfield, M.; Fromholt, D.; Copeland, N. G.; Jenkins, N. A.; Borchelt, D. R. Fibrillar inclusions and motor neuron degeneration in transgenic mice expressing superoxide dismutase 1 with a disrupted copper-binding site. *Neurobiol. Dis.* **10**:128–138; 2002.

[15] Wang, J.; Slunt, H.; Gonzales, V.; Fromholt, D.; Coonfield, M.; Copeland, N. G.; Jenkins, N. A.; Borchelt, D. R. Copper-binding-site-null SOD1 causes ALS in transgenic mice: aggregates of non-native SOD1 delineate a common feature. *Hum. Mol. Genet.* **12**:2753–2764; 2003.

[16] Wang, J.; Caruano-Yzermans, A.; Rodriguez, A.; Scheurmann, J. P.; Slunt, H. H.; Cao, X.; Gitlin, J.; Hart, P. J.; Borchelt, D. R. Disease-associated mutations at copper ligand histidine residues of superoxide dismutase 1 diminish the binding of copper and compromise dimer stability. *J. Biol. Chem.* **282**:345–352; 2007.

[17] Subramaniam, J. R.; Lyons, W. E.; Liu, J.; Bartnikas, T. B.; Rothstein, J.; Price, D. L.; Cleveland, D. W.; Gitlin, J. D.; Wong, P. C. Mutant SOD1 causes motor neuron disease independent of copper chaperone-mediated copper loading. *Nat. Neurosci.* **5**:301–307; 2002.

[18] Beckman, J. S.; Estevez, A. G.; Barbeito, L.; Crow, J. P. CCS knockout mice establish an alternative source of copper for SOD in ALS. *Free Radic. Biol. Med.* **33**:1433–1435; 2002.

[19] Bush, A. I. Is ALS caused by an altered oxidative activity of mutant superoxide dismutase? *Nat. Neurosci.* **5**:919 discussion 919–920; 2002.

[20] Son, M.; Rajendran, B.; Puttaparthi, K.; Krishnan, U.; Elliott, J. L. The effect of CCS overexpression on a transgenic mouse model of ALS. *Soc. Neurosci. Abstr.* **332**:13; 2005.

[21] Liu, H.; Zhu, H.; Eggers, D. K.; Nersissian, A. M.; Faull, K. F.; Goto, J. J.; Ai, J.; Sanders-Loehr, J.; Gralla, E. B.; Valentine, J. S. Copper(2+) binding to the surface residue cysteine 111 of His46Arg human copper–zinc superoxide dismutase, a familial amyotrophic lateral sclerosis mutant. *Biochemistry* **39**:8125–8132; 2000.

[22] Lepock, J. R.; Frey, H. E.; Hallewell, R. A. Contribution of conformational stability and reversibility of unfolding to the increased thermostability of human and bovine superoxide dismutase mutated at free cysteines. *J. Biol. Chem.* **265**:21612–21618; 1990.

[23] Porath, J.; Carlsson, J.; Olsson, I.; Belfrage, G. Metal chelate affinity chromatography, a new approach to protein fractionation. *Nature* **258**:598–599; 1975.

[24] Gaberc-Porekar, V.; Menart, V. Perspectives of immobilized-metal affinity chromatography. *J. Biochem. Biophys. Methods* **49**:335–360; 2001.

[25] Ueda, E. K.; Gout, P. W.; Morganti, L. Current and prospective applications of metal ion-protein binding. *J. Chromatogr. A* **988**:1–23; 2003.

[26] Weselake, R. J.; Chesney, S. L.; Petkau, A.; Friesen, A. D. Purification of human copper, zinc superoxide dismutase by copper chelate affinity chromatography. *Anal. Biochem.* **155**:193–197; 1986.

[27] Miyata-Asano, M.; Ito, K.; Ikeda, H.; Sekiguchi, S.; Arai, K.; Taniguchi, N. Purification of copper–zinc-superoxide dismutase and catalase from human erythrocytes by copper-chelate affinity chromatography. *J. Chromatogr.* **370**:501–507; 1986.

[28] Bush, A. I.; Multhaup, G.; Moir, R. D.; Williamson, T. G.; Small, D. H.; Rumble, B.; Pollwein, P.; Beyreuther, K.; Masters, C. L. A novel zinc(II) binding site modulates the function of the beta A4 amyloid protein precursor of Alzheimer's disease. *J. Biol. Chem.* **268**:16109–16112; 1993.

[29] Hesse, L.; Beher, D.; Masters, C. L.; Multhaup, G. The beta A4 amyloid precursor protein binding to copper. *FEBS Lett.* **349**:109–116; 1994.

[30] Carroll, M. C.; Girouard, J. B.; Ulloa, J. L.; Subramaniam, J. R.; Wong, P. C.; Valentine, J. S.; Culotta, V. C. Mechanisms for activating Cu-and Zn-containing superoxide dismutase in the absence of the CCS Cu chaperone. *Proc. Natl. Acad. Sci. USA* **101**:5964–5969; 2004.

[31] Corson, L. B.; Strain, J. J.; Culotta, V. C.; Cleveland, D. W. Chaperone-facilitated copper binding is a property common to several classes of familial amyotrophic lateral sclerosis-linked superoxide dismutase mutants. *Proc. Natl. Acad. Sci. USA* **95**:6361–6366; 1998.

[32] Bartlett, S. E.; Singala, R.; Hashikawa, A.; Shaw, L.; Hendry, I. A. Development and characterization of human and mouse specific antibodies to CuZn-superoxide dismutase (SOD1). *J. Neurosci. Methods* **98**:63–67; 2000.

[33] Moore, D. J.; Zhang, L.; Dawson, T. M.; Dawson, V. L. A missense mutation (L166P) in DJ-1, linked to familial Parkinson's disease, confers reduced protein stability and impairs homo-oligomerization. *J. Neurochem.* **87**:1558–1567; 2003.

[34] Obrig, T. G.; Culp, W. J.; McKeehan, W. L.; Hardesty, B. The mechanism by which cycloheximide and related glutarimide antibiotics inhibit peptide synthesis on reticulocyte ribosomes. *J. Biol. Chem.* **246**:174–181; 1971.

[35] Crow, J. P.; Sampson, J. B.; Zhuang, Y.; Thompson, J. A.; Beckman, J. S. Decreased zinc affinity of amyotrophic lateral sclerosis-associated superoxide dismutase mutants leads to enhanced catalysis of tyrosine nitration by peroxynitrite. *J. Neurochem.* **69**:1936–1944; 1997.

[36] Borchelt, D. R.; Lee, M. K.; Slunt, H. S.; Guarnieri, M.; Xu, Z. S.; Wong, P. C.; Brown Jr., R. H.; Price, D. L.; Sisodia, S. S.; Cleveland, D. W. Superoxide dismutase 1 with mutations linked to familial amyotrophic lateral sclerosis possesses significant activity. *Proc. Natl. Acad. Sci. USA* **91**:8292–8296; 1994.

[37] Sato, T.; Nakanishi, T.; Yamamoto, Y.; Andersen, P. M.; Ogawa, Y.; Fukada, K.; Zhou, Z.; Aoike, F.; Sugai, F.; Nagano, S.; Hirata, S.; Ogawa, M.; Nakano, R.; Ohi, T.; Kato, T.; Nakagawa, M.; Hamasaki, T.; Shimizu, A.; Sakoda, S. Rapid disease progression correlates with instability of mutant SOD1 in familial ALS. *Neurology* **65**:1954–1957; 2005.

[38] Pace, C. N.; Grimsley, G. R.; Thomson, J. A.; Barnett, B. J. Conformational stability and activity of ribonuclease T1 with zero, one, and two intact disulfide bonds. *J. Biol. Chem.* **263**:11820–11825; 1988.

[39] Furukawa, Y.; O'Halloran, T. V. Amyotrophic lateral sclerosis mutations have the greatest destabilizing effect on the apo-and reduced form of SOD1, leading to unfolding and oxidative aggregation. *J. Biol. Chem.* **280**:17266–17274; 2005.

[40] Furukawa, Y.; Torres, A. S.; O'Halloran, T. V. Oxygen-induced maturation of SOD1: a key role for disulfide formation by the copper chaperone CCS. *EMBO J.* **23**:2872–2881; 2004.

[41] Arnesano, F.; Banci, L.; Bertini, I.; Martinelli, M.; Furukawa, Y.; O'Halloran, T. V. The unusually stable quaternary structure of human Cu,Zn-superoxide dismutase 1 is controlled by both metal occupancy and disulfide status. *J. Biol. Chem.* **279**:47998–48003; 2004.

[42] Freedman, J. H.; Ciriolo, M. R.; Peisach, J. The role of glutathione in copper metabolism and toxicity. *J. Biol. Chem.* **264**:5598–5605; 1989.

[43] Krezel, A.; Wojcik, J.; Maciejczyk, M.; Bal, W. May GSH and L-His contribute to intracellular binding of zinc? Thermodynamic and solution structural study of a ternary complex. *Chem. Commun. (Camb)*704–705; 2003.

[44] Knobloch, B.; Linert, W.; Sigel, H. Metal ion-binding properties of (N3)-deprotonated uridine, thymidine, and related pyrimidine nucleosides in aqueous solution. *Proc. Natl. Acad. Sci. USA* **102**:7459–7464; 2005.

[45] Schinina, M. E.; Carlini, P.; Polticelli, F.; Zappacosta, F.; Bossa, F.; Calabrese, L. Amino acid sequence of chicken Cu, Zn-containing superoxide dismutase and identification of glutathionyl adducts at exposed cysteine residues. *Eur. J. Biochem.* **237**:433–439; 1996.

[46] Ogawa, Y.; Kosaka, H.; Nakanishi, T.; Shimizu, A.; Ohi, T.; Shoji, H.; Yanagihara, T.; Sakoda, S. Stability of mutant superoxide dismutase-1 associated with familial amyotrophic lateral sclerosis determines the manner of copper release and induction of thioredoxin in erythrocytes. *Biochem. Biophys. Res. Commun.* **241**:251–257; 1997.

[47] Jonsson, P. A.; Ernhill, K.; Andersen, P. M.; Bergemalm, D.; Brannstrom, T.; Gredal, O.; Nilsson, P.; Marklund, S. L. Minute quantities of misfolded mutant superoxide dismutase-1 cause amyotrophic lateral sclerosis. *Brain* **127**:73–88; 2004.

[48] Rakhit, R.; Cunningham, P.; Furtos-Matei, A.; Dahan, S.; Qi, X. F.; Crow, J. P.; Cashman, N. R.; Kondejewski, L. H.; Chakrabartty, A. Oxidation-induced misfolding and aggregation of superoxide dismutase and its implications for amyotrophic lateral sclerosis. *J. Biol. Chem.* **277**:47551–47556; 2002.

[49] Mukhopadhyay, C. K.; Mazumder, B.; Lindley, P. F.; Fox, P. L. Identification of the prooxidant site of human ceruloplasmin: a model for oxidative damage by copper bound to protein surfaces. *Proc. Natl. Acad. Sci. USA* **94**:11546–11551; 1997.

Acta Neuropathol (2006) 112: 52–63
DOI 10.1007/s00401-006-0056-x

ORIGINAL PAPER

Hisae Sumi · Seiichi Nagano · Harutoshi Fujimura
Shinsuke Kato · Saburo Sakoda

Inverse correlation between the formation of mitochondria-derived vacuoles and Lewy-body-like hyaline inclusions in G93A superoxide-dismutase-transgenic mice

Received: 31 May 2005 / Revised: 12 February 2006 / Accepted: 12 February 2006 / Published online: 27 April 2006

Abstract In G93A mice, the most popular model of amyotrophic lateral sclerosis (ALS), neuronal Lewy-body-like hyaline inclusions (LBHIs) and mitochondria-derived vacuoles are observed in addition to motor neuron loss. Although LBHIs are thought to be toxic, the significance of the mitochondria-derived vacuoles has not been fully investigated. In this study, the relationship between the formation of these vacuoles and LBHIs was clarified statistically in the lumbar segment from two phyletic lines of G93A mice (G1L, G1H), using immunohistochemical methods. Furthermore, the distributions of vacuoles and LBHIs were examined in the pons including the facial nucleus, where pathological changes occur in ALS patients and G93A mice. Numerous vacuoles 2–3 μm in diameter were detected in the neuropil of the lumbar segment from G1L mice euthanatized approximately 3.5 months prior to the onset of the disease. Most of the vacuoles disappeared, but some became larger as the disease progressed. The number of vacuoles with a diameter exceeding 5 μm began to decrease after disease onset, while that of intra-neuritic LBHIs increased rapidly. There was a strong inverse correlation between the numbers of vacuoles and LBHIs in symptomatic mice ($P<0.01$; G1L, $r=-0.91$; G1H, $r=-0.93$). In the facial nucleus of G1L mice, where the number of motor neurons was significantly reduced, only a few LBHIs were detected along with prominent vacuole formation. In contrast, significantly more LBHIs with little vacuole formation were evident around the facial nucleus in G1L mice. Furthermore, the SOD1 immunoreactivity in vacuoles initially increased and then decreased after disease onset. Taken together, the present findings suggest that the mitochondria-derived vacuoles might prevent the formation of LBHIs by sequestering mutated SOD1 from the cytoplasm.

Keywords Vacuole · Lewy-body-like hyaline inclusion · Mitochondria · Transgenic mice · Amyotrophic lateral sclerosis

H. Sumi (✉) · S. Nagano · H. Fujimura · S. Sakoda
Department of Neurology D-4, Osaka University Graduate School of Medicine, 2-2, Yamadaoka, Suita, 565-0871 Osaka, Japan
E-mail: hasumi@neurol.med.osaka-u.ac.jp
Tel.: +81-6-68793571
Fax: +81-6-68793579

S. Kato
Department of Neuropathology, Institute of Neurological Sciences, Faculty of Medicine,
Tottori University, Yonago, Japan

Introduction

Amyotrophic lateral sclerosis (ALS) is a fatal motor neuron disease whose pathogenesis remains unknown. About 10% of ALS cases are familial and approximately 15–20% of familial ALS patients possess the copper/zinc superoxide dismutase (SOD1) gene mutation [8, 40]. Since transgenic mice or rats carrying the human mutated SOD1 gene (SOD1 mice or rats) develop progressive motor deficits caused by loss of anterior horn cells [3, 12, 16, 32, 39, 56], they have been used by many researchers as a model of ALS. SOD1 mice or rats carrying different mutated SOD1 genes have been reported to show different pathologic features: in G93A mice or rats, many Lewy-body-like hyaline inclusions (LBHIs) and mitochondria-derived vacuoles are observed [6, 7, 32]; in G85R or G86R mice, many LBHIs, but almost no vacuoles, appear long before the onset of the disease [3, 39]; in H46R rats, many LBHIs and very few vacuoles are found [32]; in G37R mice, there is prominent vacuole formation and almost no LBHIs [55, 56]. Although in G85R mice the level of mutant G85R SOD1 protein expressed is only 20% of endogenous SOD1, these mice show very progressive motor deficits [3]. Other SOD1

mice or rats express a mutant protein level approximately 10 times higher than that in murine SOD1 [12, 16, 32, 56]. Several lines of G93A or G37R mice with different levels of mutant protein expression show different pathologic features [6, 7, 56]. Thus, the differences in neuropathology observed among SOD1 mice or rats appear to depend on the character of the mutant protein and its level of expression.

SOD1-positive LBHIs in neurons are neuropathological hallmarks of familial ALS linked with SOD1 mutation [15, 17, 22, 44]. In cell lines transfected with mutated SOD1, aggregations of mutated SOD1 or LBHI-like structures are formed [9, 21, 46]. In SOD1 mice or rats, such aggregates of SOD1 or LBHIs appear before onset of the disease [3, 4]. These aggregates of SOD1 or LBHIs, which are found specifically in the affected spinal cord or brainstem [15, 44, 54], are resistant to strong detergents or reducing agents. Although formation of aggresomes [21] or inclusions such as Lewy bodies in Parkinson's disease might be considered the result of cell-protective responses to various forms of stress [36], aggregation of mutant SOD1 or the formation of LBHIs in SOD1-mutated ALS is reported to have a toxic effect [4, 5, 23] due to sequestration of the components that are essential for maintaining cell functions [24, 25], induction of repetitive misfolding and reduction of chaperone function [2], or reduction of the activity of the proteasome integral for protein turnover [20, 21, 53].

The most important function of mitochondria in cells is the production of ATP, which is indispensable for sustaining life. Cytochrome *c* oxidase (CCO), which is located in the inner membrane of the mitochondrion and, in mammals, is composed of 13 different subunits, participates in electron transport within mitochondria [50]. Cytochrome *c* (cyt *c*) is oxidised by CCO through electron transport in the intermembrane space of the mitochondrion [38]. The large amount of energy required for action potentials in neurons depends on the ATP produced by mitochondria through electron transport. In G93A mice, the most widely used animal model of ALS, one of the very early pathologic features is the appearance of vacuoles followed by that of abnormal mitochondria [6, 14, 28, 42, 43], suggesting that the vacuoles are derived from mitochondria [14, 28].

The formation of LBHIs has been thought to have toxic effects, but the significance of the vacuoles remains unclear. Since the vacuoles appear far earlier than the LBHIs, an investigation of vacuoles would be important for clarifying the pathogenesis of the disease in G93A mice. In the study presented here, we carried out a quantitative examination of the vacuoles using an immunohistochemical method and analyzed the relationship between the vacuoles and the formation of LBHIs in the lumbar segment or facial nucleus of G93A mice in order to clarify the significance of mitochondria-derived vacuoles.

Materials and methods

Animals

Transgenic mice expressing the G93A mutated human SOD1 gene at a low (B6SJL-TgN[SOD1-G93A]1Gur^{dl}, G1L) or high (B6SJL-TgN[SOD1-G93A]1Gur, G1H) level were obtained from the Jackson Laboratory (Bar Harbor, ME, USA). These mice were bred and maintained as hemizygotes by mating with wild-type B6SJL mice. Non-transgenic littermates were used as controls. All animals were genotyped using polymerase chain reaction amplification of the tail DNAs under conditions that have been described previously [33]. All animals were handled in accordance with the Guidelines for the Care and Use of Laboratory Animals at Osaka University Graduate School of Medicine. We evaluated the animals clinically, examining their hindlimb extension when they were suspended in the air by the tail [1, 33, 34, 49].

Tissue preparation

We examined control (260 ± 6 days old), G1L, and G1H mice ($n = 3$ in each group). G1L mice were euthanatized at the age of 90, 140 (the asymptomatic stage), 180 (the presymtomatic stage), 230 days (the symptomatic stage) or at the end stage when they could hardly move or drink water because of severe paralysis (259 ± 6 days old, the moribund state). G1H mice were euthanatized at the age of 66 (the asymptomatic stage), 100 (the early symptomatic stage), or 115 days (the late symptomatic stage). They were deeply anesthetized with sodium pentobarbital, and perfused with phosphate-buffered saline (PBS, pH 7.4) followed by 4% paraformaldehyde. The brainstem and spinal cord were removed, immersed in the same fixative overnight at 4°C, and then cryoprotected. Ten-micrometer-thick frozen sections were prepared and stained with hematoxylin and eosin (HE). Small pieces of lumbar segments were fixed with 2.5% glutaraldehyde in 0.1 M PB (pH 7.4) for 2 h at 4°C, followed by 1% osmium tetroxide in 0.1 M PB at 4°C, dehydrated in an ethanol series and embedded in Epon; LUVEAK-812 (glycerol triglycidyl ether, Nakarai Tesque, Kyoto, Japan)/LUVEAK-DDSA (dodecylsuccinic anhydride, Nakarai Tesque)/LUVEAK-MNA (methylnadic anhydride, Nakarai Tesque)/LUVEAK-DMP-30 (2,4,6-Tris (dimethylaminomethyl) phenol, Nakarai Tesque). Transverse sections 1 μm thick were stained with toluidine blue.

Immunohistochemical analysis of vacuoles in lumbar segment and brainstem

For immunohistochemical evaluations, frozen or deparaffinized sections were incubated for 30 min with

0.3% H_2O_2 to quench endogenous peroxidase activity and then washed with PBS. Normal goat serum was used as a blocking reagent. Mouse monoclonal antibodies against cyt *c* (1:100 in 1% PBS containing bovine serum albumin, clone 6H2.B4, BD PharMingen, CA, USA), CCO subunit I (1:400 clone 1D6, Molecular Probes Inc, OR, USA), human SOD1 (0.5 μg/ml, clone 1G2, MBL, Aichi, Japan) or GFAP (ready to use, DAKO, Glostrup, Denmark) were used as primary antibodies. Tissue sections were incubated with each primary antibody for 18 h at 4°C. The avidin–biotin–immunoperoxidase complex (ABC) method was employed according to the manufacturer's instructions to detect each bound antibody using the appropriate Vectastain ABC kits (Vector Laboratories, Burlingame, CA, USA). 3,3′-Diaminobenzidine tetrahydrochloride (DAKO, Glostrup, Denmark) was used as the final chromogen. Hematoxylin was used to counterstain cell nuclei. In control experiments, primary antibodies were omitted from the incubation medium.

Quantitative evaluation of motor neurons, LBHIs and cyt *c*-positive vacuoles in the lumbar segment

To estimate the number of neurons in the gray matter (VII, VIII, IX Rexed areas) showing clear nucleoli and cell bodies with a diameter greater than 25 μm [26, 28, 48], presumed to be alpha motoneurons [10, 30, 31], video images of the anterior horns were obtained with a digital camera (KEYENCE VB-7010, KEYENCE, Osaka, Japan) attached to a light microscope (ECLIPSE E800, Nikon, Tokyo, Japan) for each section, and the areas of motor neurons showing clear nucleoli and cell bodies were measured using image analysis software (VH-H1A5, KEYENCE). The number of neurons with a diameter greater than 25 μm were counted in HE-stained sections. LBHIs with a halo and core and cyt-*c*-positive vacuoles in the gray matter were also counted (×100 objective). LBHIs were also confirmed using antibodies against human SOD1 and GFAP. Since the vacuoles are contained exclusively in neuronal processes [19, 43], and not in astrocytes, only neuronal LBHIs were counted to examine the relationship between the vacuoles and LBHIs in neurons. LBHIs in cells possessing glial nuclei were omitted. To establish how the size and number of vacuoles in the lumbar segments of G1L mice changes chronologically over the clinical course of the disease, vacuoles were divided according to size into small (< 5 μm) or large (> 5 μm). Every fifth section (40 μm interval) was obtained, and three sections from each mouse were used to obtain the total number of neurons, LBHIs or vacuoles. The quantitative evaluation was analyzed statistically. Moreover, the relationship between the number of vacuoles and LBHIs was estimated in each symptomatic mouse (G1L, 230 days and the moribund state 259 ± 6 days; G1H, 100 and 115 days).

Quantitative analysis of LBHIs in the pons including the facial nucleus

For histological analyses of the facial nucleus (nVII), we examined non-transgenic littermates ($n = 3$, 264 ± 7 days) and G1L mice in the moribund state ($n = 7$, 258 ± 7 days). Each carefully hemisected brainstem was embedded in paraffin and sectioned transversely. The pons including the nVII was identified in these sections, with reference to the mouse brain atlas of Paxinos and Franklin [37]. Six-micrometer-thick paraffin sections were prepared and stained with HE. In the nVII, large neurons with clear nucleoli and cell bodies were counted. LBHIs located in three subregions of the pons (vacuole-rich area = intra-nVII, the border zone, and vacuole-poor area, as delineated in Fig. 1) were also counted (×40 objective). To estimate the number of LBHIs per unit area in each subregion, video images of the pons were obtained with a digital camera (KEYENCE VB-7010, KEYENCE, Osaka, Japan) attached to a light microscope (ECLIPSE E800, Nikon, Tokyo, Japan) for each section, and the areas of three subregions were measured using image analysis software (VH-H1A5, KEYENCE). Every fifth section (at 24-μm intervals)

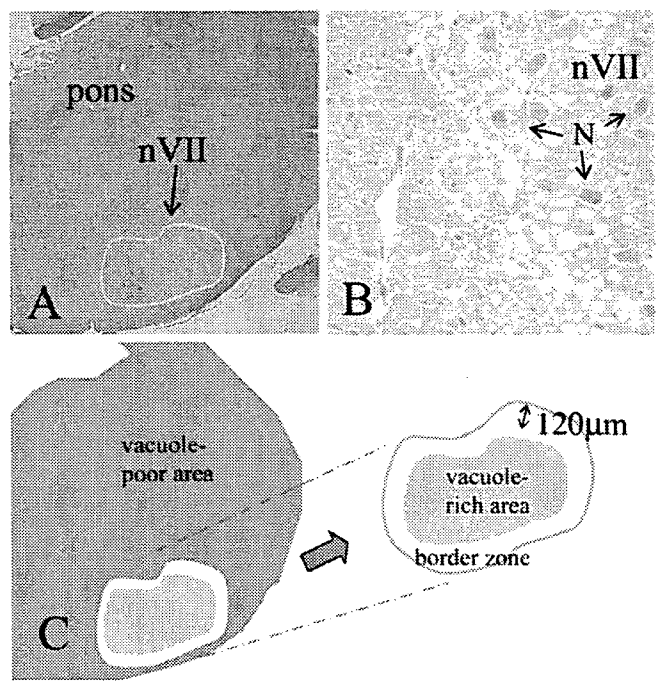

Fig. 1 Schematic diagram of the three subregions in the pons; vacuole-rich area (= intra-nVII), the border zone and vacuole-poor area. The boundary of massive vacuole formation limited to the facial nucleus (nVII) is shown at low (**a**) and high (**b**) magnification as a *yellow line*, using actual microscopic fields digitized for illustrative purposes. The definition of the vacuole-rich area (= intra-nVII), border zone and vacuole-poor area is as follows: vacuole-rich area (*light blue*) corresponds to the inner area outlined in *yellow*; the border zone (*white*) corresponds to the surrounding area outlined in *yellow and green*, 120 μm exterior to the *yellow line*; the vacuole-poor area (*pink*) corresponds to the outer area of the pons excluding the other two regions. *N* neuron

was obtained, and three sections from each mouse were used to obtain the total number of neurons and the density of LBHIs. The number of motor neurons and the density of LBHIs were analyzed statistically. All quantitative investigations were performed independently by three neuropathologists (HS, HF, SK).

Statistics

Data are expressed as the mean ± standard error of the mean (SEM). All statistical analyses of histopathological data were carried out using the Statview for Macintosh software package (Ver5.0, SAS Institute Inc, CA, USA). A nonparametric test, Mann–Whitney *U* test, was used to analyze the number of neurons, LBHIs and vacuoles in the lumbar segment or the number of neurons and the density of LBHIs in the pons. The relationship between the number of LBHIs and vacuoles in the lumbar segment was estimated by regression analysis.

Results

Morphological changes of vacuoles in the lumbar segment of G1L or G1H mice

Many tiny vacuoles 2–3 μm in diameter were found in neurites mainly at the edge of the anterior horn in G1L mice at 90 days (Fig. 2a). Some of the vacuoles were hardly distinguishable from capillary vessels. At 140 days, larger but fewer vacuoles than those at 90 days were observed in the same area (Fig. 2b). Vacuoles were also scattered diffusely in the anterior horn. At 180 days, round vacuoles larger than those at 140 days (Fig. 2c) were frequently found throughout the gray matter. At the later stages in G1L mice, the large vacuoles appeared slightly deformed and were reduced in number (Fig. 2d). Many LBHIs were scattered in the gray matter. In G1H mice, more prominent vacuole formation was observed (Fig. 4a, d) than that in G1L mice. The vacuoles became larger and their number was reduced by 115 days (Fig. 4d) in comparison with those at 100 days (Fig. 4a). Although at 100 days the vacuoles were observed mainly in the anterior horn, by 115 days their distribution had also extended to the whole of the gray matter.

Immunohistochemical analyses of vacuoles in the lumbar segment of G1L mice

As a negative control, sections were incubated without the primary antibody; this resulted in no staining in the lumbar segments of normal and G93A low-copy transgenic mice (G1L mice). As expected, the cytoplasm of motor neurons was clearly stained for cyt *c* or CCO in the lumbar segment of normal mice (Fig. 3a, b). The staining pattern with the two antibodies was similar, showing a fine granular pattern. The neuropil was also weakly stained for these antibodies. The immunohistochemical analysis revealed many tiny vacuoles, strongly positive for cyt *c* at the edge of the anterior horn in G1L mice (90 days; Fig. 3c–e). Some vacuoles were scattered in the neuropil of the anterior horn. Axons were lined with tiny vacuoles that appeared to be attached together. The rim of the vacuoles in the neuropil was stained for cyt *c* (Fig. 3d, e). The structures lying interior to the vacuolar rim were CCO-positive, although the rim itself was CCO-negative. At 140 days, the number of vacuoles was lower than that at 90 days. In contrast, large vacuoles (> 5 μm), which were never seen at 90 days, were frequently observed at the edge of the anterior horn (Fig. 3f). The cyt *c* immunoreactivity was reduced within the rim of these large vacuoles (Fig. 3f, g). Small vacuoles (< 5 μm) did

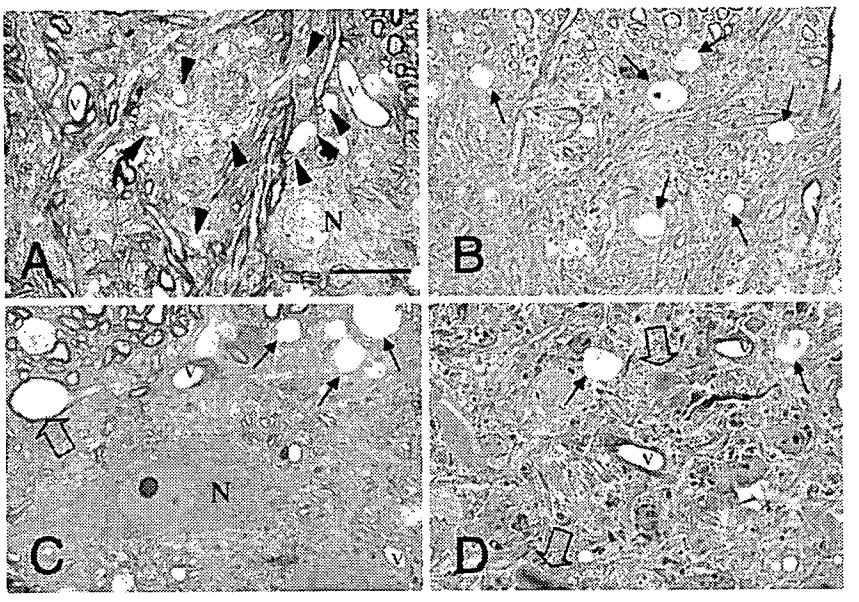

Fig. 2 Morphological changes in vacuoles in the anterior horn of G1L mice at different stages. (Epon sections, toluidine blue, **a** 90 days, **b** 140 days, **c** 180 days, **d** end stage). **a** Many small vacuoles (< 5 μm, *arrow heads*) are evident at the edge of the anterior horn. **b** The number of vacuoles has decreased. Vacuoles (*arrows*) at the edge of the anterior horn have become larger. **c** The number of vacuoles (*arrows*) is smaller than in **b**. Note the large vacuoles in neurites including axons (*clear arrow*). **d** Only a few vacuoles (*arrows*) are evident. LBHIs (*clear arrow*) appear in the anterior horn. *N* neuron; *V* vessels. Scale bar **a** (also for **b–d**) 20 μm

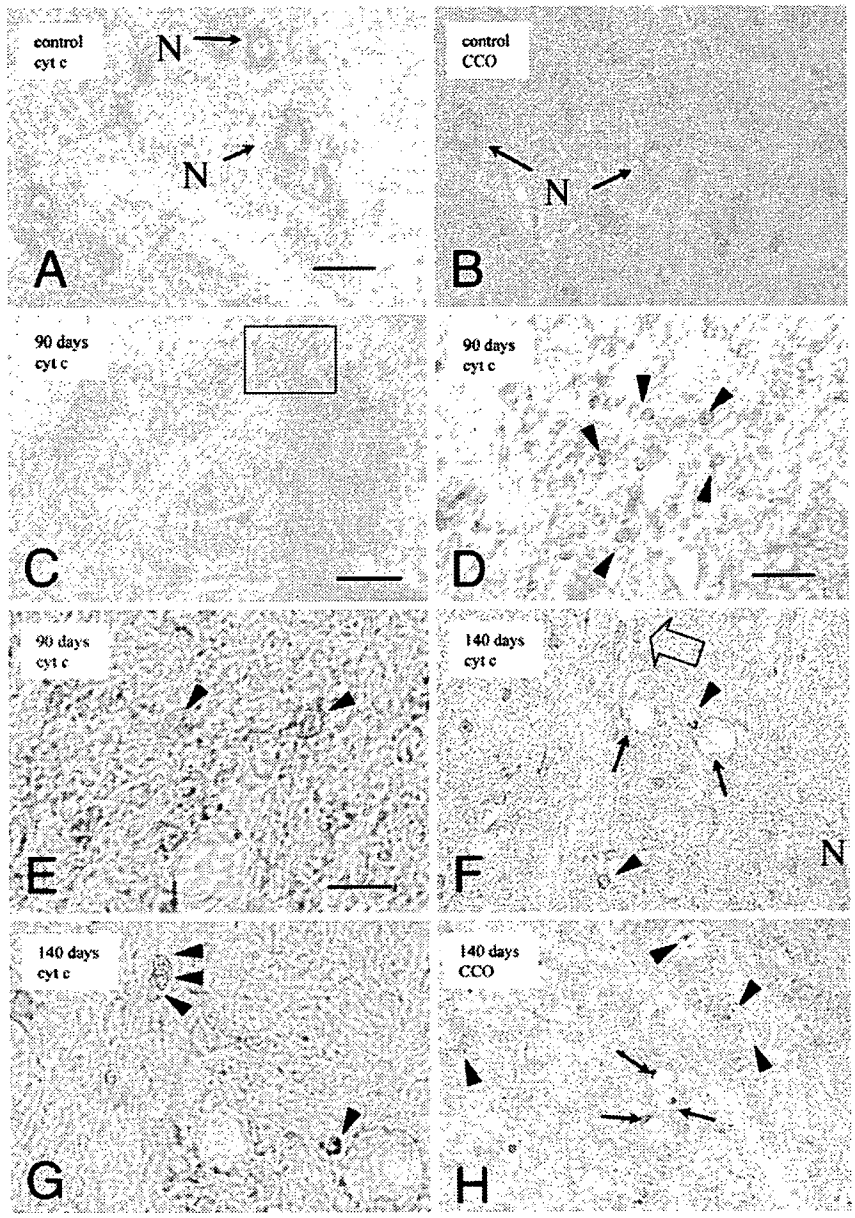

Fig. 3 Immunohistochemistry of vacuoles in the anterior horn of G1L mice (**a**, **b** normal control, **c**–**l** G1L mice; **a**, **b** 263 days, **c**–**e** 90 days, **f**–**h** 140 days, **i** 180 days, **j**, **k** 230 days, **l** end stage; **a**, **c**–**g**, **j**, **l** cyt *c*, **b**, **h**, **i**, **k** CCO). **a** A fine granular staining pattern is evident in the cytoplasm of motor neurons (*N*, *arrows*). The neuropil is also weakly stained. **b** Motor neurons (*N*, *arrows*) show well-defined cytoplasmic staining for CCO. Diffusely scattered fine dots can be seen in the neuropil. **c**–**e** Tiny, densely immunolabeled vacuoles within the rim (*arrow heads*) are prominent at the edge of the anterior horn. **d** is a high magnification view of **c**. **e** is a high magnification view of **d**. **f** The number of vacuoles is lower than in **d**. Large vacuoles (> 5 μm, *arrows*), which were never seen in **d**. The immunoreactivity for cyt *c* is reduced within the rim of large vacuoles (*arrows*) compared to that of small vacuoles (< 5 μm, *arrow heads*). In axons, tiny vacuoles are tightly packed to form a columnar shape (*clear arrow*). **g** is a high magnification view of **f**. **h** Abnormal structures lying interior to the rim of vacuoles (*arrows*, *arrow heads*) are strongly positive for CCO. Irregular CCO-positive dots (*arrow heads*) are scattered in the neuropil. **i** Large CCO-positive complexes lying interior to the rim of large vacuoles. **j** The number of vacuoles (*arrow*, *arrow head*) is lower than that in **i**. Cyt-*c*-positive small vacuoles (*arrow head*) are seen only rarely. **k** CCO-positive complexes (*arrows*) lying interior to the vacuolar rim have become atrophic in comparison with those in **i**. **l** Small vacuoles are not evident. Some large vacuoles (*arrows*) remain. *N* neurons; *V* vessels. Scale bars: **a** (also for **b**)50 μm, **c** 100 μm, **d** (also for **f**, **h**–**l**) 20 μm, and **e** (also for **g**) 10 μm

not fuse to form a large vacuole. Some small and large vacuoles were found in the dorsal horn. Each vacuole had CCO-positive structures lying interior to the rim (Fig. 3h). At 180 days, there was a reduction in the number of small vacuoles (< 5 μm), and many large vacuoles (> 5 μm) were found scattered not only at the edge of the anterior horn, but also throughout the neuropil. These vacuoles had highly CCO-positive structures lying interior to the rim (Fig. 3i). At later stages, the tiny, strongly cyt *c*-positive vacuoles were